

# Bulletin of Volcanology

## Reconstruction of total grain size distribution of the climactic phase of a long-lasting eruption: the example of the 2008-2013 Chaitén eruption.

--Manuscript Draft--

|  |  |
|--|--|
| <b>Manuscript Number:</b>                          | BUVO-D-16-00019R2  |
| <b>Full Title:</b>                                 | Reconstruction of total grain size distribution of the climactic phase of a long-lasting eruption: the example of the 2008-2013 Chaitén eruption.  |
| <b>Article Type:</b>                               | Research Article   |
| <b>Corresponding Author:</b>                       | Fabrizio Alfano<br>Arizona State University<br>UNITED STATES   |
| <b>Corresponding Author Secondary Information:</b> |  |
| <b>Order of Authors:</b>                           | Fabrizio Alfano<br>Costanza Bonadonna<br>Sebastian Watt<br>Charles Connor<br>Alain Volentik<br>David Pyle  |
| <b>Funding Information:</b>                        |  |
| <b>Abstract:</b>                                   | <p>The 2008-2013 eruption of Chaitén volcano (Chile), was a long-lasting eruption whose climactic phase (May 6th 2008) produced a sub-Plinian plume, with height ranging between 14 to 20 km, that dispersed to the NE, reaching the Atlantic coast of Argentina. The erupted material was mainly of lithic origin (77wt%), resulting in a uni-modal Total Grain-Size Distribution (TGSD) dominated by coarse ash (77wt%), with <math>M_{dof}</math> of 2.7 and 2.4. Lapilli clasts (&gt; 2 mm) dominate the proximal deposit within ~20 km of the vent, while coarse (63 <math>\mu</math>m-2mm) and fine ash (&lt;63 <math>\mu</math>m) sedimented as far as 800 km from vent, generating mostly poly-modal grain-size distributions across the entire deposit. Given that most of the mass is sedimented in proximal areas, results show that possible contributions of later explosive events to the thickness of the distal deposit where layers are less distinguishable (&gt;400 km) do not significantly affect the determination of the TGSD. In contrast, gaps in data sampling in the medial deposit (in particular the gap between 50 and 350 km from vent, that coincides with shifts in sedimentation regimes) have large impacts on estimates of TGSD. Particle number distribution for this deposit is characterized by a high power-law exponent (3.0) following a trend very similar to the vesicle size distribution in the juvenile pyroclasts. Although this could be taken to indicate a bubble-driven fragmentation process, we suggest that fragmentation was more likely the result of a shear-driven process, because of the predominance of non-vesicular products (lithics and obsidians) and the large fraction of coarse ash in the TGSD.</p> |
| <b>Response to Reviewers:</b>                      | see attachment   |

[Click here to view linked References](#)

**Reconstruction of total grain size distribution of the climactic phase of a long-lasting eruption: the example of the 2008-2013 Chaitén eruption.**

Fabrizio Alfano<sup>1</sup>, Costanza Bonadonna<sup>2</sup>, Sebastian Watt<sup>3</sup>, Chuck Connor<sup>4</sup>, Alain Volentik<sup>4#</sup>, David M. Pyle<sup>5</sup>

1. School of Earth and Space exploration, Arizona State University, Tempe, AZ (USA)

2. Department of Earth Sciences, University of Geneva, Geneva (Switzerland)

3. School of Geography, Earth and Environmental Sciences, University of Birmingham, Birmingham (U.K.)

4. University of South Florida, Tampa, FL (USA)

5. Department of Earth Sciences, University of Oxford (U.K.)

# Now at: ExxonMobil Exploration Company, Spring, TX (USA)

Corresponding Author:

Fabrizio Alfano

Arizona State University, School of Earth and Space Exploration

POBOX 876004

Tempe, AZ 85282-1404

email: [fabrizio.alfano@asu.edu](mailto:fabrizio.alfano@asu.edu)

Phone: 1-480-727-3578

Version: 17 May 2016

## Abstract

The 2008-2013 eruption of Chaitén volcano (Chile), was a long-lasting eruption whose climactic phase (May 6th 2008) produced a sub-Plinian plume, with height ranging between 14 to 20 km, that dispersed to the NE, reaching the Atlantic coast of Argentina. The erupted material was mainly of lithic origin (~77 wt%), resulting in a uni-modal Total Grain-Size Distribution (TGSD) dominated by coarse ash (77 wt%), with  $Md_\phi$  of 2.7 and  $\sigma_\phi$  of 2.4. Lapilli clasts (> 2 mm) dominate the proximal deposit within ~20 km of the vent, while coarse (63  $\mu$ m - 2 mm) and fine ash (<63  $\mu$ m) sedimented as far as 800 km from vent, generating mostly poly-modal grain-size distributions across the entire deposit. Given that most of the mass is sedimented in proximal areas, results show that possible contributions of later explosive events to the thickness of the distal deposit where layers are less distinguishable (>400 km) do not significantly affect the determination of the TGSD. In contrast, gaps in data sampling in the medial deposit (in particular the gap between 50 and 350 km from vent, that coincides with shifts in sedimentation regimes) have large impacts on estimates of TGSD. Particle number distribution for this deposit is characterized by a high power-law exponent (3.0) following a trend very similar to the vesicle size distribution in the juvenile pyroclasts. Although this could be taken to indicate a bubble-driven fragmentation process, we suggest that fragmentation was more likely the result of a shear-driven process, because of the predominance of non-vesicular products (lithics and obsidians) and the large fraction of coarse ash in the TGSD.

## Introduction

Volcanic explosive eruptions inject large amounts of pyroclastic material into the atmosphere, which is widely dispersed downwind from the volcano. The physical characteristics of the tephra

and of the associated deposits are closely related to the characteristics of volcanic eruptions that produced them (e.g., magnitude and style of the eruption, plume dynamics and rise, conduit dynamics and magma fragmentation). Therefore, a detailed study of individual pyroclasts and associated deposits can provide critical insights into volcanic processes and can inform forecasts of future eruptions (Houghton and Wilson 1989; Cashman and Mangan 1994; Bonadonna et al 2005; Bonadonna and Houghton 2005; Costantini et al 2010; Alfano et al 2011a; Rust and Cashman 2011; Alfano et al 2012).

Volcanic particles originate from the fragmentation of fresh magma (juvenile clasts) and are typically ejected from the eruptive vent together with lithic clasts, resulting from the disruption of conduit and/or crater walls (Cas and Wright 1988). All clasts are injected into the atmosphere and are transported laterally under the action of the spreading cloud and the prevailing winds, and eventually sediment on the ground. Fallout processes mostly depend on particle size, with the largest particles sedimenting rapidly, and the smallest particles remaining suspended in the atmosphere for longer time periods, and sedimenting up to several hundreds of kilometres from the vent (Watt et al 2009; Alfano et al 2011a; Durant et al 2012). As a result, the character of tephra deposits varies significantly with the distance from the vent, as a function of plume height and wind patterns (Walker 1971; Carey and Sparks 1986, Pyle, 1989).

Ideally, the grain size distribution (GSD) of a tephra sample can be described using a log-normal function characterized by a median, which represents the median diameter of particles comprising the grain size distribution ( $Md_\phi$ ), and a sorting value ( $\sigma_\phi$ ), which describes the dispersion of the distribution from the  $Md_\phi$  (Inman 1952). GSDs are often more complex than implied by these two parameters, presenting multiple modes and skewed distributions. These

complexities arise from a broad range of processes, including size-selective sedimentation processes (e.g. particle aggregation, convective instabilities; Carey and Sigurdsson 1982; Durant et al 2009; Manzella et al 2015), different density distributions of pyroclasts of different origins (i.e., lithics vs juvenile), and/or additional fragmentation (e.g. comminution in pyroclastic density currents, PDCs) and sedimentation processes (e.g., co-PDC plumes) (Eychenne et al 2012; Watt et al 2015; Eychenne et al 2015). As a result, the dynamics of volcanic eruptions and fragmentation processes can only be fully understood in terms of the total grain size distribution (TGSD) of tephra deposits, which is typically difficult to characterize. TGSD also represents a critical eruption source parameter necessary for accurate numerical simulations of eruption forecasting (Mastin et al 2009; Folch 2012), and, therefore, systematic sensitivity analysis of its determination and representativeness are essential (e.g., Bonadonna and Houghton 2005; Volentik et al 2010; Durant et al 2012; Eychenne et al 2012; Bonadonna et al 2015; Tsunematsu and Bonadonna 2015; Costa et al 2016).

The determination of TGSD requires a combination of detailed and widespread sampling of the deposit and dedicated statistical strategies for the averaging of individual GSD analysis that can deal with the non-uniform distribution of measurement sites (e.g., Voronoi tessellation (Bonadonna and Houghton 2005)). TGSDs are often characterized by complex functions, resulting from the combination of two or more subpopulations associated with multiple fragmentation processes and/or the fragmentation of heterogeneous material (Kaminski and Jaupart 1998; Volentik et al 2010; Rust and Cashman 2011; Dufek et al 2012; Bonadonna et al 2015; Eychenne et al 2015). Numerous theoretical and experimental studies have shown how the fragmentation process can be described by fractal fragmentation theory, which approximates the TGSD of the deposit using power-law functions (Turcotte 1986; Kueppers et al 2006b; Perugini

and Kueppers 2012; Costa et al 2016). In this approach, the slope of the trend (as plotted on a log-log plot) represents the fractal dimension of the deposit, and the fractal dimension increases with the potential energy of the fragmentation process (Perugini and Kueppers 2012).

In this work we provide a further characterization of the climactic phase of the 2008-2009 eruption of Chaitén volcano of May 6th, 2008 (Folch et al 2008; Watt et al 2009; Alfano et al 2011b), which largely affected populations and economic activities as far away as the coast of Argentina, 600 - 800 km from the volcano. The long duration, the broad footprint of tephra dispersal, the widespread impact on surrounding communities and critical infrastructures (Wilson et al 2012), and the rhyolitic composition of the magma make this eruption of particular interest. Prior attempts to reconstruct TGSD of the Chaitén eruption used only distal data (e.g., Watt et al 2009; Durant et al 2012; Osoreo et al 2013). In this work, we present a characterization of GSD and componentry observed in the proximal area (up to 20 km away from the vent) and combine them with the characteristics of the distal deposit presented by Watt et al. (2009). Our final goal is to reconstruct a TGSD that is representative of the entire deposit originating from the May 6th explosive phase of the 2008 Chaitén eruption and to provide insights into the fragmentation processes during this event based on fractal analysis.

### **The 2008-2013 eruption of Chaitén volcano (Chile)**

The eruption of Chaitén volcano on May 2008 interrupted a 400-year period of quiescence (Watt et al 2011; Amigo et al 2013; Lara et al 2013). The volcano was not monitored and generally considered inactive, so sparse geophysical data are available, the only exception being the seismic data recorded by the regional network. These seismic data do not provide detailed information about the onset of the eruption and the very first period of activity, when most

explosive phases occurred (Carn et al 2009; Lara 2009; Alfano et al 2011b). As a result, most of the information about this eruption comes from remote sensing retrievals (Carn et al 2009; Watt et al 2009) and field observations of the volcanic deposit and products (Castro and Dingwell 2009; Martin et al 2009; Watt et al 2009; Alfano et al 2011b; Alfano et al 2012; Durant et al 2012; Lara et al 2013; Major et al 2013; Pierson et al 2013).

The eruption started during the night between May 1st and May 2nd, 2008, producing a first explosive phase during which about 0.5 km<sup>3</sup> of pyroclastic products were erupted and dispersed over a wide area, reaching the Atlantic coast of Argentina (Watt et al 2009; Alfano et al 2011b; Durant et al 2012). This variably explosive phase lasted for approximately 10 days, with a climax on May 6th, when a sub-Plinian explosive phase produced a 18-20 km high, dark-grey sustained plume (based on remote sensing; Carn et al 2009) that deposited a tephra layer of about 0.3 km<sup>3</sup> NE of the vent (Alfano et al 2011b). Geophysical observation indicate that on May 12th the extrusion of a new rhyolitic dome started, ending the initial explosive phase of the eruption (Lara 2009, Alfano et al 2011b). The proximal deposit consists of a complex sequence of individual layers with grain size ranging from lapilli to ash, and occasional large bomb-sized pumices. The upper layers are typically up to a few centimetres thick, and are often discontinuous and cannot be followed throughout the entire deposit. In contrast, the tephra deposit associated with the climactic event of May 6th 2008 (layer  $\beta$ , Alfano et al 2011b), which is at the base of the stratigraphic sequence, is a massive lapilli-clast layer with thickness up to 17 cm (~ 5 km from the vent). Tephra samples of layer  $\beta$  include three main components that were identified in previous studies of this eruptive event (Castro and Dingwell 2009; Alfano et al 2011b; Alfano et al 2012; Castro et al 2012). The most frequent component is represented by grey blocky and foliated clasts, poorly vesicular, finely crystalline, and occasionally with a

reddish colour due to alteration. These clasts are rhyolitic and interpreted as lithic material derived from disruption of the pre-existing lava dome (Alfano et al 2011b; Alfano et al 2012). The second and third components, which account for smaller proportions of the deposit compared to the lithic fraction, are represented by non-altered obsidian fragments and highly vesicular, aphyric, sub-angular pumices (Castro and Dingwell 2009; Alfano et al 2011b; Alfano et al 2012; Castro et al 2012). These two components are interpreted as juvenile products, as they have similar rhyolitic composition (i.e. 74.18 and 74.11 SiO<sub>2</sub> wt% for pumices and obsidians, respectively; Alfano et al 2011b). Field evidence indicates that these two components were erupted simultaneously (Castro et al 2012).

The climactic explosive event of May 6th was characterized by the rapid rise and the violent fragmentation of a volatile-rich magma batch triggered by a sudden decrease of pressure (10 MPa s<sup>-1</sup>) associated with the failure of the pre-existing obsidian dome (Alfano et al 2012). The second phase of the eruption was characterized by the extrusion of an obsidian dome and episodic small Vulcanian explosions with associated plumes and PDCs (Alfano et al 2011b; Major et al 2013).

The products of the first phase of the explosive activity were mainly deposited in Argentina, to the East of the volcano, between May 1st and May 13th. This phase was characterized by several explosive events, producing plumes with height above 10 km. Watt et al. (2009) identified a SE lobe, correlated with the activity between May 1st and May 5th, and a NE lobe correlated with the activity of May 6th (Watt et al 2009; Alfano et al 2011b). However, several eruptive events (May 2nd, 7th, 8th and 10th) produced fallout sedimentation in the same area as the May 6th explosion (Martin et al 2009; Watt et al 2009; Osores et al 2013). After May 13th, activity



shifted to a less explosive style, events became less intense and produced smaller plumes (< 10 km high) that left no significant deposits in Argentina (Watt et al 2009).

## **Methodology**

### *Deposit characterization, componentry, grain size and particle density*

The proximal tephra samples of the May 6th climactic phase of the 2008-2013 Chaitén eruption (Layer  $\beta$ ; Alfano et al 2011b) were collected between 3 and 20 km from the vent in January 2009 (Fig. 1). Grain-size and componentry analysis were partly carried out in situ (down to 8 mm diameter), and partly in the laboratory, using an optical stereoscopic microscope (on grain size between 2 and 0.5 mm) and a SEM (JEOL JSM7001F) on grain size smaller than 0.5 mm at the University of Geneva.

Grain-size analyses were conducted by dry sieving down to 0.5 mm ( $\phi = 1$ ) for 22 samples separating the products in full  $\phi$  classes ( $-\log_2$  of particle diameter in mm). The coarse fraction (i.e. diameter  $\geq 8$  mm;  $\leq -3\phi$ ) was sieved in situ in order to reduce the possible breakage of coarse clasts, modifying the original GSD. The size fraction  $> 0\phi$  (i.e. diameter  $< 0.5$  mm) was analysed using a laser diffraction grain-sizer (CILAS 1180; <http://www.cilas.com/>) down to  $10\phi$  (i.e. 1  $\mu\text{m}$ ). The combination of the dry sieving analyses and laser diffraction analyses was carried out as described by Eychenne et al (2012). The GSD measured through laser diffraction, expressed in volume %, was converted into mass % using the density of particles in each grain size class. The variation of particle density with grain size was determined using a high precision water pycnometer (Fig. 2). These analyses were carried out on ash samples with particle sizes between 2 mm and 250  $\mu\text{m}$ , following the methodology described by Eychenne and Le Pennec (2012). The lowest grain-size limit for density analysis was imposed by the scarce fraction of

fine ash in the samples; the density of particles smaller than 250  $\mu\text{m}$  was assumed constant due to their low and homogeneous vesicularity (Bonadonna and Phillips 2003; Alfano et al 2011a). The resulting mass distribution was then scaled to the mass fraction of the size class analysed (<0.5 mm), obtaining the final GSD of each analysed sample. Results were analysed using KWare SFT 2.22.0170<sup>1</sup> (Wohletz et al 1989) to determine median and sorting coefficient (i.e.,  $Md_\phi$  and  $\sigma_\phi$ ; Inman 1952) and deconvolved to identify subpopulations and their relative proportions. GSD analysis was carried out by deconvolving the distribution using log-normal functions, following the procedure of Wohletz et al (1989) and optimizing the results until the sum of the fractions of the subpopulation equalled 1. Results were compared with the grain size parameters of the samples of the distal deposit (Watt et al 2009). Componentry was determined for 11 samples located along the dispersal axis (cf., Fig. 1) to a distance of ~25 km by hand-picking individual clasts down to 0.5 mm. More than 75 wt% of the whole sample was processed in each case.

#### *Total grain size distribution*

TGSD was determined by applying the Voronoi tessellation method (Bonadonna and Houghton 2005) on the combined dataset of Alfano et al. (2011b) and Watt et al. (2009) using a dedicated MATLAB code (Biass and Bonadonna 2014) and assuming that the isoline of zero mass corresponded to the 0.1 mm isopach (Watt et al 2009; Alfano et al 2011b). However, the combination of the two datasets does not produce uniform coverage of the fallout deposit. In fact, GSD data are missing for three relatively large sectors: a medial area (Z1, 20-140 km from the vent), a medial/distal area (Z2, 260-380 km from the vent), and a distal area (Z3, 570-770 km

---

<sup>1</sup><http://www.ees.lanl.gov/geodynamics/Wohletz/SFT.htm>

206 from the vent). In order to assess the representativeness of the resulting TGSD, selected synthetic  
 207 GSD data were extrapolated based on observed features of proximal and distal deposits and  
 208 added to the total dataset before application of the Voronoi tessellation strategy, following a  
 209 similar approach introduced by Bonadonna et al. (2015) for the tephra deposit associated with  
 210 the 2011 Cordón Caulle eruption. The extrapolation was based on the estimation of  $Md_\phi$  and  $\sigma_\phi$ ,  
 211 and the fractions of lapilli ( $X_l$ ;  $64 \text{ mm} > d > 2 \text{ mm}$ ), coarse ( $X_c$ ;  $2 \text{ mm} > d > 64 \mu\text{m}$ ) and fine ( $X_f$ ;  
 212  $< 64 \mu\text{m}$ ) ash at specific locations. First, thematic maps describing the variation of  $Md_\phi$ ,  $X_l$ ,  $X_c$   
 213 and  $X_f$  through the deposit were compiled;  $\sigma_\phi$  is nearly constant for all samples (i.e., standard  
 214 deviation of the  $\sigma_\phi$  values is 0.4). Therefore, we considered  $\sigma_\phi$  to be constant for the entire  
 215 deposit and equal to  $1.7\phi$  (average of the  $\sigma_\phi$  of all GSD). Second, the extrapolated values of  $Md_\phi$ ,  
 216  $X_l$ ,  $X_c$  and  $X_f$  were used to determine a synthetic GSD at the selected locations. Sensitivity  
 217 analyses were also carried out to estimate the number of synthetic points required to obtain stable  
 218 results, and to assess the relative influence of different portions of the deposit (i.e. Z1, Z2, Z3  
 219 and Z1+ Z2) on the TGSD determination (details on the synthetic GSD determination and  
 220 sensitivity analysis are described in the appendix). Finally, in order to assess the potential  
 221 contribution of later explosive events to the distal tephra deposit associated with the Chaitén  
 222 climactic phase, TGSD was also calculated reducing the mass load measured at distances  $>150$   
 223 km from the vent (i.e. for all measurement sites beyond the proximal region) to 80% and 60% of  
 224 their original value. This is justified by examination of GSD in the distal 6th May deposit, which  
 225 shows clear bimodality, with a dominant coarse mode assumed to represent the 6th May deposit  
 226 (accounting for 50 – 80% of the deposit at individual sites) and a finer mode which may partly  
 227 reflect deposition of tephra from additional explosive phases (e.g. phases on May 2nd and May

8th; Fig. 3). As a result, eight distinct datasets were compiled and used to calculate the TGSD (Table 1).

#### *Determination of particle number distribution*

Particle number distribution (PND) was assessed to obtain insights into the fragmentation process (Turcotte 1986; Kaminski and Jaupart 1998; Kueppers et al 2006a; Kueppers et al 2006b; Rust and Cashman 2011; Perugini and Kueppers 2012) using the method described by Kaminski and Jaupart (1998). The number of particles of a given grain size class ( $N_\phi$ ) is the ratio between its mass ( $M_\phi$ ) and the mass of the average fragment representing that class ( $m_\phi$ ):

$$N_\phi = \frac{M_\phi}{m_\phi} = M \frac{C_\phi}{V_\phi \cdot \rho} \quad (1)$$

where  $M$  is the total mass and  $C_\phi$  is the fraction % of the  $\phi$  grain-size class; the value of  $m_\phi$  was determined by multiplying the volume ( $V_\phi$ ) of the average fragment (assumed to be a sphere with diameter equal to the mid-interval between two grain size classes) and the average fragment density ( $\rho$ ). PND was determined for individual samples (GSD-PND) and for the total deposit (TGSD-PND).

GSD-PND cannot be calculated following eq. 1 because a value of total mass for an individual sample is not easy to define. Therefore, GSD-PND was calculated as the number of particles included in 1 m<sup>3</sup> of sample. The associated mass was obtained multiplying the unit volume by the density of the deposit (i.e., 1250 kg/m<sup>3</sup> for the proximal area (Alfano et al 2011b), and 997 kg/m<sup>3</sup> for the distal area (Watt et al 2009)). As the mass of a unit volume is known, GSD-PNDs can be obtained following eq. 1. The resulting GSD-PND trends were then combined using a convolution approach to estimate a PND referenced to the entire deposit (Conv-PND). This methodology calculates the average  $N_\phi$  of individual samples. For lapilli clasts, with grain size

between  $1\phi$  and  $-6\phi$  (2-64 mm), only the samples in the proximal deposit were considered; for fine ash, with grain size  $> 4\phi$  ( $< 63 \mu\text{m}$ ), only the samples of the distal deposit were considered; for coarse ash, with grain size between  $1\phi$  and  $4\phi$  (2 mm –  $63 \mu\text{m}$ ), samples of the proximal and distal deposit were both considered. The resulting convolution was then multiplied by the total volume of the deposit ( $1.8 \times 10^{-1} \text{ km}^3$ ; Alfano et al, 2011b) to obtain the distribution of the total number of particles and compare it with the PND derived from the Voronoi TGSD. TGSD-PND was calculated considering a total mass equal to  $2.3 \times 10^{11} \text{ kg}$  (obtained by multiplying the total volume by the deposit density; Alfano et al 2011b) and the TGSD obtained using the Voronoi method. As a result, the Conv-PND and TGSD-PND both represent the absolute number of particles of a given grain-size class in the entire tephra deposit. GSD-PND, Conv-PND and TGSD-PND were plotted on a log-log plot of the number of particles against the equivalent particle diameter and fitted with a power-law function to determine the relative exponent describing the distribution (Kaminski and Jaupart 1998; Kueppers et al 2006a; Perugini and Kueppers 2012).

## **Results**

### *Characterization of the tephra deposit*

The componentry characteristics of the fine-ash fraction was qualitatively analysed based on SEM images (Fig. 3). We found the fine fraction in the samples is mainly composed of poorly-vesicular blocky grains. Due to the fine grain-size of this material, it is difficult to discriminate between components in all cases, but the angular nature, low to absent vesicularity and finely crystalline nature of many clasts suggests that the lithic component makes up a major proportion of these samples. Vesicular clasts are also frequent, but in most cases these clasts are sparsely

274 vesicular. Highly vesicular pumice clasts are rare. Fine glass fragments, likely originating from  
 275 bubble wall disruption, and sometimes with star-shaped morphology, are common, and likely  
 276 represent glass formed in the interstices of bubbles. This latter set of clasts is interpreted as  
 277 representing juvenile components.

278 In the distal deposit (i.e. all measurement sites in Argentina; Fig.3), individual layers,  
 279 corresponding to the proximal stratigraphy, were not observable. However, deposits derived  
 280 from individual explosive phases can be inferred by comparing the lobate deposit distribution  
 281 with satellite imagery of the transport direction of individual explosive phases (Fig.3a). This  
 282 demonstrates that the northerly lobe of the deposit results from the 6th May explosion, with  
 283 possible additional contributions from the May 2nd and May 8th explosive phases. Assuming  
 284 that our interpretation of layer  $\beta$  as the proximal 6th May deposit is correct, then we can combine  
 285 grain-size information from the distal northern lobe with the proximal layer  $\beta$ , to derive a total  
 286 grain-size distribution for the 6th May event.

287 The nature of the distal 6th May deposit is best considered by comparison with additional lobes  
 288 in the distal deposit. Figure 3b compares the grain-size distributions at a distance of ~150 km  
 289 between the 3rd, 2nd/5th and 6th May lobes. The unimodality of the 3rd and 2nd/5th May  
 290 deposits, with a mode at ~4 phi, contrasts strongly with the bimodal 6th May deposit, with a  
 291 narrow, coarser mode at 1.5 phi. The 6th May sample has a secondary mode at ~4 phi, and it is  
 292 plausible that this sub-population represents deposits from the 2nd or 8th of May. In this  
 293 interpretation, the 6th of May event deposited the narrow coarse mode. This represents by far the  
 294 coarsest ash observed in the Argentinean sample set, and supports our interpretation of this  
 295 material being derived from the 6th May explosion, which was the most powerful stage of the  
 296 eruption. Building on this interpretation, we consider the grain-size distribution of samples

further down-wind in the northerly lobe. Again, samples can be characterised by two sub-populations, and we attribute the coarsest sub-population to the 6th of May event, which indicates rapid fining of this deposit in a down-wind direction (Fig. 3c). Some of the finer sub-populations within this part of the tephra deposit may also originate from the 6th May plume (e.g. via aggregation processes), but we cannot discard an origin from other phases of the eruption (e.g., May 2nd or 8th). No direct evidence of particle aggregation was observed within the deposit itself (Watt et al., 2009).

SEM images of ash from the different eruption lobes show similar morphologies and vesicularity patterns across all parts of the distal deposit (Fig. 3d). The 6th of May deposit at site 06-16 (150 km from the vent) shows that the coarse mode comprises angular, dense to sparsely vesicular fragments, and similar material dominates the coarse mode further downwind, at site 07-20 (215 km from the vent). Similar characteristics define samples in the 3rd May lobe (samples 05-07, 80 km from the vent, and sample 05-22, 160 km from the vent; Fig. 3d). Although sparsely to moderately vesicular particles are common, highly vesicular pumice clasts are uncommon, although they do occur as a minor component in all samples (Watt et al., 2009). It is harder to determine the nature of the finer fractions, which have an angular morphology that in some cases is consistent with bubble-driven fragmentation, but may also plausibly be produced by other fragmentation processes. In general, the observations of distal ash morphologies support the proximal observations of a predominance of relatively dense (i.e. non- to sparsely-vesicular) clasts over the highly vesicular pumice component within the deposit.

The analysis of the density of the juvenile products of layer  $\beta$  (i.e., pumices, obsidian and density of the solid fraction obtained by analysing powdered pumices) was carried out by Alfano et al (2012). Here, we completed the density analysis for the fine fraction. The Dense Rock

Equivalent (DRE) density of the juvenile products is equal to  $2240 \pm 14 \text{ kg/m}^3$ , very close to the DRE density of the obsidian fragments ( $2270 \pm 30 \text{ kg/m}^3$ ), whereas the density of pumice clasts (determined on individual clasts with diameter  $> 4 \text{ cm}$ ) is  $700 \pm 160 \text{ kg/m}^3$  (Alfano et al. 2012). Density of bulk samples, for particles in the size range between  $2 \text{ mm}$  and  $250 \mu\text{m}$ , was found almost constant. Density values vary between  $1960 \pm 270 \text{ kg/m}^3$  (for particles with diameter between  $250$  and  $360 \mu\text{m}$ ) and  $2280 \pm 25 \text{ kg/m}^3$  (for particles with diameter between  $1$  and  $2 \text{ mm}$ ) (Fig. 2). Although it would be expected for larger clasts to show lower density values than the finer, the difference in the measurements is smaller than their uncertainty, and therefore it is safe to assume that the density has a small, perhaps insignificant, variation with grain size. We assume a particle density of  $2140 \pm 170 \text{ kg/m}^3$ , which is the average of the density measured throughout the entire grain size interval.

#### *Grain-size distribution and componentry*

GSD of individual samples of the May 6th proximal deposit is complex, mostly showing polymodality (Fig. 4). GSDs are characterized by a main sub-population with a mode between  $1.0\phi$  and  $-2.7\phi$  ( $0.5 - 6.5 \text{ mm}$ ), and a relatively small standard deviation ( $1-2\phi$ ). This sub-population accounts for  $> 71 \text{ wt\%}$  of the unit. The remainder can be divided into two additional sub-populations: a coarse sub-population, which represents about  $20 \text{ wt\%}$  of the samples that consists of particles in the size range between  $-5.3\phi$  and  $0.8\phi$  with a small standard deviation ( $\sim 1\phi$ ); and a fine sub-population, which represents up to  $8 \text{ wt\%}$  of the samples, that consists of particles in the range  $0.6\phi$  to  $6.5\phi$ , with a larger standard deviation ( $1-4\phi$ ). Samples F23 and F24 are the exception, for which the fine sub-population represents  $20 \text{ wt\%}$  and  $28 \text{ wt\%}$  of the whole sample, respectively.



Componentry analyses show a dominance of the lithic fraction representing  $76.6 \pm 3.4$  % of the whole sample (Fig. 4); the juvenile fraction represents  $23.4 \pm 3.4$  %, being roughly equally divided between obsidian fragments ( $51.8 \pm 9.3$  %) and pumices ( $48.2 \pm 9.3$  %). We can infer that most of tephra in the proximal deposit is not vesicular (lithics and obsidian fragments being  $88.6 \pm 3.3$  % in mass). The vesicular fraction, represented by pumices, is estimated to be about  $11.4 \pm 3.3$  %. As a result, aforementioned sub-populations include particles of all identified componentry categories, and therefore are not simply related to grain density.

$Md_\phi$  and  $\sigma_\phi$  of the proximal deposit have been plotted with respect to distance from the vent and compared with the values of the distal deposit from Watt et al (2009) (Fig. 5). This plot shows the sampling gap in the medial area (~20-120 km from the vent; Fig 5a).  $Md_\phi$  decreases with distance from vent following a power-law trend, varying between  $-2.7\phi$  and  $1.0\phi$ , in the proximal area, and  $1.7\phi$  and  $5.0\phi$ , in the distal area (Fig. 5a);  $\sigma_\phi$  remains roughly constant, with average value of  $1.7 \pm 0.4$  (Fig. 5b).  $Md_\phi$  and  $\sigma_\phi$  plot consistently in the field of fallout deposits (Fig. 5b).

The coarse subpopulation mode falls in proximity of the main population (bulk)  $Md_\phi$ , but is better sorted. The fine subpopulation shows similar grain-size characteristics of the distal ash, but falls partially outside of the top-right limit of the fallout domain suggested by Walker (1971) (Fig. 5b).

### *Total grain-size distribution*

Figures 6 and 7 show the grain-size variation of the proximal and distal tephra deposit, respectively, in terms of  $Md_\phi$  and fraction of lapilli, coarse ash and fine ash. The proximal deposit is coarse (i.e.  $Md_\phi < 1$ ; Fig. 6a) and dominated by lapilli-sized clasts (up to  $150 \text{ kg/m}^2$ ; Fig. 6b), with a minor fraction of coarse ash (up to  $50 \text{ kg/m}^2$ ; Fig. 6c) and a relatively negligible

366 fraction of fine ash ( $1\text{--}2\text{ kg/m}^2$ ; Fig. 6e). The distal deposit is mostly composed of coarse and fine  
 367 ash with  $Md_\phi > 1$  ( $d < 2\text{ mm}$ ; Fig. 7).  
 368 Figure 8 describes the decay trends of the grain-size parameters over the whole deposit.  $Md_\phi$   
 369 increases with the distance from the vent as a result of the decrease of particle grain size  
 370 following two exponential decay fitting trends (regression lines:  $Md_\phi = 0.2x - 4.4$ ,  $R^2 = 0.96$ ;  
 371  $Md_\phi = 0.003x + 1.2$ ;  $R^2 = 0.99$ ; Fig. 8a), with a significantly faster rate up to about 27 km from  
 372 the vent (i.e., break-in-slope in Fig. 8a). Lapilli fragments occur only in the proximal area, as the  
 373 mass load decreases rapidly with the distance from the vent, reaching zero at about 40–50 km  
 374 (regression line:  $y = 1.8 \cdot 10^3 e^{-0.269x}$ ,  $R^2 = 0.93$ ; Fig. 8b). Therefore, no lapilli are expected to be  
 375 observed in the medial area. Coarse ash is distributed through the entire deposit, having a very  
 376 rapid decay in the proximal area up to about 48 km from the vent (break-in-slope in Fig. 8c), and  
 377 decaying very gradually in the distal area (regression lines:  $y = 94 e^{-0.081x}$ ,  $R^2 = 0.99$ ;  $y = 2 e^{-0.004x}$ ,  $R^2 = 0.99$ ). Finally, fine ash is dispersed mainly in the distal area and is characterized by an  
 378 exponential decay trend that follows the decay trend of coarse ash (regression line:  $y = 2.5 e^{-0.004x}$ ,  $R^2 = 0.97$ ; Fig. 8d).  
 379  
 380  
 381 As mentioned above, the TGSD was reconstructed both for the original dataset (dataset A) and  
 382 for additional datasets including various synthetic points coinciding with sampling gaps in the  
 383 medial deposit (datasets B to F) and various reductions of mass/area values associated with the  
 384 distal deposits to account for possible contribution of later explosive events (datasets G and H)  
 385 (Fig. 9 and appendix). The TGSD associated with datasets A (original dataset) and B (accounting  
 386 for data interpolation within sampling gaps) show significant differences (Fig. 9b). Dataset A  
 387 ( $Md_\phi = 3.6$ ;  $\sigma_\phi = 2.5$ ) results in a strongly bi-modal TGSD, with similar fraction of coarse (49 %) and fine (41 wt%) ash, and a minor amount of lapilli (10 wt%). The bimodality becomes less  
 388

pronounced in the TGSD of dataset B, which is also slightly coarser ( $Md_{\phi} = 2.6$ ;  $\sigma_{\phi} = 2.5$ ; Fig. 10). In fact, the fraction of coarse ash is higher (62 wt%), while the fraction of both fine ash and lapilli is lower (29 wt% and 9 wt%, respectively).

In order to assess the effect of the addition of synthetic points, TGSD was also calculated for reduced datasets and compared with dataset B (Figs 9 and 10) in order to evaluate the weight of the three zones Z1, Z2 and Z3 in the calculation. The tessellation map implemented to show the absolute mass associated with individual polygons indicates that the three zones include a significant portion of the mass of the deposit (up to  $> 10^6$  kg) (Fig. 9a). In particular, we have sequentially removed the points of Z1 (dataset C), Z2 (dataset D), Z3 (dataset E), and both points of Z1 and Z2 (dataset F) from dataset B (cf., Table 1). Results indicate that the lack of observations in all the areas can influence the calculations. In fact, TGSD from dataset C ( $Md_{\phi} = 2.9$ ;  $\sigma_{\phi} = 2.4$ ) results in an underestimation of coarse ash (- 4.6 wt%) and an overestimation of fine ash (+ 3.4 wt%), whereas there is no significant variation for lapilli (+ 1.2 wt%). TGSD from dataset D ( $Md_{\phi} = 2.7$ ;  $\sigma_{\phi} = 2.5$ ) results in a similar underestimation of coarse ash (-4.9 wt%) and larger overestimation of fine ash (+ 4.6 wt%), with almost no major variation in the lapilli fraction (+ 0.3 wt%). TGSD from dataset E ( $Md_{\phi} = 2.7$ ;  $\sigma_{\phi} = 2.5$ ) does not result in significant variation of coarse and fine ash fractions (-1.8 wt% and + 1.5 wt% respectively), nor of the lapilli fraction (+ 0.8 wt%). TGSD from dataset F ( $Md_{\phi} = 3.3$ ;  $\sigma_{\phi} = 2.0$ ) is significantly different, with large underestimation of coarse ash (- 10.3 wt%) and overestimation of fine ash (+ 8.8 wt%) and a small overestimation of the lapilli fraction (+ 1.5 wt%).

The possible influence of the amalgamation of products from multiple individual explosive phases (i.e. deposits from May 2nd and May 8th within the same region as the May 6th event) was investigated. In order to account for possible increase of the mass load in the distal area due

to amalgamation of multiple ash layers, the values of mass/area of the distal points (beyond about 150 km from vent) was reduced to 80 wt% (dataset G) and 60 wt% (dataset H). The TGSD results do not show significant variation from the TGSD obtained using dataset B (Fig. 9 and 10), with associated  $Md_{\phi}$  values of  $2.5\phi$  and of  $2.4\phi$  for both datasets, and variation in the relative fractions of lapilli, coarse and fine ash  $< 5$  wt%.

#### *Particle number distributions*

Power-law best fits of GSD-PND of distal deposits are characterized by exponents slightly higher than those associated with the proximal deposit, with an average value of  $2.6 \pm 0.3$  (average exponent of proximal and distal deposit is  $2.4 \pm 2.5$  and  $2.7 \pm 0.2$ , respectively) (Fig. 11a). In addition, the TGSD-PND associated with dataset A and B, and Conv-PND (obtained through convolution of GSD-PNDs of dataset A) are characterized by very similar power-law exponents (2.9, 3.1 and 3.0 for Conv-PND and TGSD-PND of datasets A and B, respectively; Fig. 11b). TGSD-PND of dataset B also shows a good correlation with the vesicle size distribution (VSD; Fig. 11c).

#### **Discussion**

The long-lasting eruption of May 2008-August 2013 of Chaitén volcano produced rhyolitic tephra that dispersed over an area of about  $4 \cdot 10^5$  km<sup>2</sup>; about 0.3 km<sup>3</sup> of material was erupted during the climactic event of May 6th (i.e., total volume erupted is estimated to be about 1 km<sup>3</sup>; Watt et al 2009; Alfano et al 2011b; Bonadonna and Costa 2012). The climactic event was characterized by a sub-Plinian sustained column that, according to a new estimation based on the

distribution of the maximum lithic fragments<sup>2</sup> (Carey and Sparks 1986), results in a plume height of 14 km (above sampling height, a.s.h.; between sea level and 700 m a.s.l.), which is lower than both the original estimation of 19 km a.s.h. of Alfano et al (2011b), and the evaluation based on remote sensing (20 km above sea level) (Carn et al 2009). This lower plume height estimate is likely related to the fact that the 3.2 cm isopleth contour is associated with sedimentation from plume margins (e.g., Bonadonna et al 2013). In contrast, the remote sensing observation is more likely associated with the peak intensity of the eruption.

#### *Componentry of the Chaitén 2008 eruption*

Layer  $\beta$ , attributed to the May 6th explosion, is composed mainly of non-vesicular fragments of lithic origin ( $77 \pm 3$  wt%) associated with a minor juvenile fraction composed equally of non-vesicular obsidian fragments and pumices. As a result, the products of this explosion are almost entirely composed of non-vesicular dense products, i.e. lithic and obsidian clasts (~89 wt%). The predominance of non-vesicular fragments explains the constant particle density across grain size classes (cf. Fig. 2). The dominance of a relatively dense fraction throughout the May 6th deposit is supported by examination of the distal ash deposit, which is dominated by dense and sparsely vesicular clasts, inferred to correspond with the lithic fraction observed in the proximal Layer  $\beta$ . In the proximal area, Layer  $\beta$  is distinctive, and defined by a much coarser grain size than overlapping deposits from additional eruptive phases. The fragments within this coarse population are angular and dense to sparsely vesicular, showing no significant vertical gradation. These characteristics support our interpretations that relate the eruption dynamics of the May 6th explosion to the disruption of the pre-existing rhyolitic dome (Alfano et al 2012), producing a

---

<sup>2</sup> This estimation corrects and updates the previous estimation of Alfano et al. (2011b) and is based on the isopleth map presented in the same work. In the previous version the estimate was erroneous due to an overestimation of the downwind limit of the 3.2 cm isopleth.

relatively short-lived eruptive column ( $< 2$  hours; Alfano et al 2011b). It is however, interesting to note that earlier phases of the distal deposit (e.g. May 3rd lobe, Fig.3d) share similar characteristics to the May 6th deposit, with highly vesicular clasts being rare throughout the distal ash samples, suggesting that a juvenile component may have been a relatively minor constituent to much of the initial and most explosive phases of the Chaitén eruption. As mentioned earlier, the new dome started growing only after May 12th (Lara 2009, Alfano et al 2011b), so that the non-vesicular material must belong to the previous dome.

Tephra deposits in the proximal area are characterized by poly-modal grain-size distributions. De-convolution using SFT identified the presence of a main sub-population combined with a coarser and a finer sub-population (cf., Fig. 4). The coarse sub-population is probably related to fallout from plume margins. In fact, a plume of about 14-20 km above the vent is associated with a corner position (transition between vertical plume and horizontal cloud) of about 5 km from vent based on the theoretical relation of Bonadonna and Phillips (2003). Considering that our sample locations of the proximal deposit are located between 3 and 20 km from the vent, many of them (cf., Fig. 2) can be considered representative of the plume-margin fallout. This corresponds to the first break-in-slope observed in the thinning decay of the tephra deposit (i.e.  $\sim 4$  km; Alfano et al. 2011b). The fine sub-population represents a small fraction of the bulk sample ( $> 10$  wt%), with the exception of two samples (F23 and F24) located at the northern margin of the tephra deposit ( $> 10$  km from the vent; cf. Fig. 1). The presence of a fine grained sub-population could be associated both with a co-PDC component (e.g., Eychenne et al 2012) and with size-selective processes, such as particle aggregation and convective instabilities (e.g., Brown et al 2010; Carazzo and Jellinek 2013; Manzella et al 2015; Durant 2015). PDCs were documented but, based on the damage produced to vegetation, were considered to be

characterized by low energy and small runout distances (between 0.7 and 6 km from the vent; Major et al 2013). These characteristics suggest that the co-PDC ash represents a negligible or small contribution to the total tephra deposit. In contrast, the higher fraction of the fine sub-population observed for the two samples in the northern margin of the fallout deposit (F23 and F24) and the coarse and fine ash decay trends (cf., Fig. 6 and 7), suggest that size-selective processes (e.g., aggregation) might have had a significant role in the sedimentation of the products. The decay trend of fine ash mostly follows the decay trend of coarse ash, but there is the caveat that the fine sub-population in this region is potentially the product of earlier or later eruption phases (May 2nd and May 8th; Figure 3), making it difficult to reach unequivocal conclusions. In fact, the overall thinning trends do not show significant deviations from typical exponential trends which could be related to size-selective sedimentation processes (e.g. particle aggregation, convective instabilities). However, size-selective sedimentation processes have already been observed to occur even without strong evidence in the deposit (as when aggregates are fragile they are typically not preserved in the deposit; (e.g., Bonadonna et al 2002; Bonadonna et al 2011) and when the thinning trend is not significantly affected (e.g. Bonadonna and Phillips, 2003).

#### *Reconstructing the TGSD of the whole deposit*

Long-lasting explosive eruptions can result in complex tephra deposits that, due to the multiple explosive pulses and the wide dispersal of the products, are difficult to characterize. The May 6th sub-Plinian event represents the climactic phase of the 2008-2013 Chaitén long-lasting eruption, and, therefore, the reconstruction of the associated TGSD requires an accurate correlation between proximal and distal deposits. In addition, the proximal and the distal deposits were

collected independently and present large sampling gaps (i.e., Watt et al 2009; Alfano et al 2011b). The deposit associated with the climactic phase could be well characterized in proximal areas based on stratigraphic evidences (layer  $\beta$  of Alfano et al. 2011b); however the proximal stratigraphy is not evident in distal area (beyond 120 km from vent), but could be identified based on changing wind patterns, which produced discrete lobes of deposition (Watt et al 2009). Considering that the climactic phase had the highest plumes and the largest dispersal of the whole 2008-2013 eruption, with a cloud spreading NE, we assume that it was associated with the coarsest subpopulation within the NE depositional lobe, as described by Watt et al. (2009) (c.f. Fig3). Nonetheless, we cannot exclude the possibility that additional explosive events also contributed to the sedimentation of the NE lobe, particularly in the finer sub-populations. In addition, a minor portion of the products (at fine-ash grain sizes) were lost due to sedimentation into the ocean. These challenges in unambiguously and fully characterising a discrete May 6th distal deposit could introduce some errors in estimates of both erupted mass and TGSD for the May 6th deposit.

Alfano et al. (2011b) carried out a sensitivity analysis on the calculation of the erupted mass, showing that small uncertainties in the (mm-scale) deposit thickness over the distal region, arising from the above issues, does not result in significant errors in volume estimates. Here, we further investigated the effect of these issues on the determination of the TGSD. Our results show that reducing the thickness of the distal May 6th deposit (beyond 150 km from vent) to 80% and 60% of the original value does not produce significant variation in the fraction of coarse and fine ash (< 5%) in the TGSD. This is likely due to the fact that most of the mass is deposited in proximal to medial areas, and, therefore, a small variation of the distal deposit thickness does not significantly affect the determination of either erupted mass nor TGSD. We



525 want to stress that our results do not imply that amalgamation of products of different explosive  
 526 events in a tephra deposit is irrelevant, but that a critical interpretation of tephra deposits is a  
 527 crucial aspect of the characterization of eruptive parameters, such as erupted mass and TGSD.  
 528 Finally, we also explored the effect of sample distribution on the determination of TGSD. The  
 529 May 6th explosion was characterized by a relatively short duration ( $> 2$  h) and produced a  
 530 massive deposit, without any significant vertical gradation (Alfano et al 2011b). Therefore, the  
 531 main parameter influencing the determination of the TGSD is the areal distribution of the sample  
 532 points. In particular, 22 samples and 42 samples were studied for grain-size data in proximal and  
 533 distal areas, respectively (cf., Fig. 1, 6 and 7). Such a sample distribution covers most of the  
 534 dispersal area of the Chaitén eruption climactic (May 6th) phase, with gaps between 20 and 120  
 535 km from vent (Z1), 260 and 380 km from vent (Z2), and 580 and 760 km from vent (Z3) (cf., Fig  
 536 5a and 9b). Even though the Voronoi Tessellation method is designed to deal with non-uniform  
 537 distributions, our results show how the lack of samples in a large part of the deposit can  
 538 influence the final TGSD. In fact, the Voronoi tessellation applied to the original dataset results  
 539 in a bimodal distribution, in which fine ash represents the largest fraction (i.e.,  $Md_{\phi} = 3.6$ ,  $\sigma_{\phi} =$   
 540  $2.5$ ), while the Voronoi tessellation applied to the original dataset combined with 9 synthetic  
 541 points (dataset B) reduces the bimodality and shifts the distribution towards the coarse ash (i.e.,  
 542  $Md_{\phi} = 2.6$ ,  $\sigma_{\phi} = 2.5$ ; cf.; Fig. 9b). In particular, the gaps associated with the sectors Z1 and Z2  
 543 influence greatly the TGSD calculation, as they coincide with an area of inferred high  
 544 accumulation of coarse ash fallout (Figs 8 and 9a). As a result, the presence of these two  
 545 sampling gaps creates a shift of the TGSD towards the fine ash (i.e.,  $Md_{\phi} = 3.2$ ,  $\sigma_{\phi} = 2.0$ ; cf., +  
 546  $14.4$  wt%; cf., Fig. 10), and underestimates the coarse ash fraction ( $- 16.2$  wt%). The Voronoi  
 547 strategy cannot capture this shift in fallout regime and results in a bimodal distribution, which is

very likely not related to the eruption dynamics but to an artefact of the sample distribution. A similar approach was also applied for the characterization of the TGSD associated with the 2011 Cordón Caulle eruption, for which most distal data were missing (Bonadonna et al 2015). However, the TGSD of the Cordón Caulle eruption associated with the addition of distal synthetic data did not result in significant difference from the original dataset. These results mirror the results obtained calculating the TGSD using dataset E. The GSD that can be observed at the margins of the distal region is probably nearly constant, and therefore fewer datapoints can be enough for a reliable TGSD computation. On the other hand, in the medial/distal region, where the GSD can present greater variations, the presence of sampling gaps can be critical and compromise the calculation of the TGSD. Based on these results, we suspect that the previously published TGSDs (i.e.,  $5\phi > Md\phi > 3\phi$ ; Watt et al 2009; Osóres et al 2013) result in the underestimation of the coarse ash fraction as a result of the use of an incomplete dataset, lack of proximal data and with sampling gaps, and the possible inclusion, however not in large proportion, of fine ash originated from other eruptive events (i.e., May 2nd and May 8th; cf., Fig. 3).

#### *Insights into fragmentation process from grain size observations*

TGSD results (i.e. dataset B in Fig. 9b) show that the May 6th 2008 Chaitén explosion was characterized by the generation of a large amount of ash ( $d < 2$  mm), representing 98 wt% of the products, mainly falling in the size range of the coarse ash ( $2$  mm  $> d > 63$   $\mu$ m; 77 wt%). The associated TGSD-PND is characterized by a power-law exponent (3.0), falling in the lower end of the range typically described for fallout deposits (i.e., 3.0-3.7; Kaminski and Jaupart 1998). The PND trends are concave downwards (cf., Fig. 11), which is typically observed in many PND

(Kaminski and Jaupart 1998; Rust and Cashman 2011; Costa et al 2016). The significance of this trend has been related to the possible underestimation of values at the extremes of the distribution. However, the goodness of fitting ( $R^2 = 0.99$ ) indicates that the concavity observed in our result is statistically not significant. In fact, the Log-Log plot used to study these distributions smoothes possible complexities that are evident in the GSD plots (cf., Fig. 3d and 4). As a result, PND is not a suitable tool to characterize the complexity of the fragmentation process as a whole (e.g. bimodality), yet is a very effective tool to compare different eruptions and to characterize the energy involved in the explosive process based on power-law functions (Kueppers et al 2006a; Kueppers et al 2006b; Perugini and Kueppers 2012).

TGSD-PND also follows the VSD trend (cf., Fig. 11c), suggesting a relationship between grain size and vesicularity (Rust and Cashman 2011). However, most of the products are the result of the fragmentation of non-vesicular material (89%), mainly from the pre-existing wall and dome rocks. The textural analyses carried out on pumice samples describes the vesicularity of the juvenile products as characterized by a unimodal distribution with mode falling between 0.05 and 0.13 mm (Alfano et al 2012). TGSD is characterized by  $Md_{\phi}$  values equal to 0.16 mm (cf., 2.6 $\phi$ ), which is slightly coarser than the modal range identified for the vesicles. Generally, a bubble-driven ash-generation process produces clasts that are roughly of the same range of dimensions as the vesicles (Rust and Cashman 2011; Genareau et al 2012; Genareau et al 2013). This consideration suggests that vesicularity had only a secondary role in magma fragmentation, limited to the minor vesicular juvenile fraction, and might have been responsible for the production of most of the fine-ash fraction.

However, if vesiculation is not the main factor driving the energy of the sub-Plinian May 6th event, this raises the question of what drove the violent and efficient fragmentation in the May

6th explosion, given the large proportion of ash generated in the event. Previous studies on rhyolitic eruptions (e.g., Chaitén and Cerdón Caulle) have demonstrated that despite the high silica content, rhyolitic magmas can have lower viscosity than expected. In fact, a rhyolitic magma stored in a shallow magmatic chamber can maintain near-liquidus hydrous conditions (Castro and Dingwell 2009; Castro et al 2013; Jay et al 2014), and the viscosity can be low enough to allow for a fast ascent through the crust (Wicks et al 2011). The Chaitén eruption was characterized by an apparently very rapid onset, favoured by the low viscosity of the rhyolitic magma, that could rise rapidly and drive fracturing of the confining wall rock/pre-existing lava dome (Castro and Dingwell 2009; Wicks et al 2011). In these conditions, magma was likely characterized by a high shear rate that, associated with a high decompression rate ( $\sim 10$  MPa/s; Alfano et al 2012), and this could have acted as the main factor driving the violent fragmentation of the magma and the pre-existing dome. The dominance of coarse ash in the TGSD and the relatively low exponent of the PND trend suggest that fragmentation was relatively less efficient than other explosive eruptions that may perhaps be more dominantly driven by vesiculation. Yet, the production of a 15-20 km sub-Plinian column suggests that high shear and decompression rate may still produce sufficient energy and ash content to produce a highly explosive, buoyant eruption column, even if that material involved is dominated by non-juvenile material. Based on our result and on previous work, we suggest that a better understanding of the link between fragmentation dynamics, ash production, explosive energy, proportion of juvenile products and the associated TGSD is required.

## Conclusions

Based on our detailed grain-size characterization of the tephra deposit associated with the May 6th 2008 Chaitén eruption, we can conclude that:

- 1) Regardless of the similarities between TGSD and PND with pumice vesicularity, the erupted products of the climactic phase of the Chaitén eruption were probably the result of a shear-driven fragmentation that mostly acted on the material of the old obsidian dome. In fact, a bubble-driven fragmentation process is not compatible with the high proportion of lithic material (76%) in the proximal deposit.
- 2) The proximal tephra deposit (3-20 km from vent) consists of both uni- and poly-modal, mostly well-sorted GSDs with  $Md_{\phi}$  and  $\sigma_{\phi}$  varying between  $-2.6-1.2\phi$  and  $0.9-3$ , respectively. De-convolution of the GSD identified a main subpopulation dominated by coarse ash and lapilli ( $> 71$  wt% of the samples) with modes between  $0.8\phi$  and  $-2.7\phi$  ( $0.5 - 8.0$  mm) (probably associated with the fallout from the umbrella cloud), a smaller lapilli-rich subpopulation ( $<20$  wt%) with modes between  $-5.3\phi$  and  $0.8\phi$  (probably related to the sedimentation from plume margins), and a fine ash-rich subpopulation (up to 28 wt%) with modes between  $0.6\phi$  and  $6.5\phi$ , (probably mostly related to size-selective sedimentation processes such as aggregation or convective instabilities).
- 3) The proximal deposit is composed mainly of lithic fragments ( $76.6 \pm 3.4$  wt%) and a smaller fraction of juvenile fragments ( $23.4 \pm 3.4$  wt%); the juvenile fraction comprises highly vesicular aphyric pumice and non-vesicular obsidian fragments in almost equal proportions; the lithic fraction is composed of laminated grey rhyolitic fragments originated by the disruption of the old dome. This conclusion is supported by the dominance of dense to sparsely vesicular fragments that comprise the coarsest (May 6th) fraction of the distal deposit. Highly vesicular pumice is rare in this deposit, but notably it

is also rare in other lobes of the distal deposit, formed from earlier phases of the Chaitén eruption, which are also dominated by relatively dense clasts. Our results suggest consistency in the componentry of the ash fraction between proximal and distal samples.

4) The decay trends of both  $Md_\phi$  and coarse ash can be described by two exponential segments on semi-log plots, with break-in-slope located at 16 and 31 km from the vent, respectively, possibly reflecting relevant shifts in the sedimentation regime in this area. In contrast, both the decay trend of lapilli and fine-ash fragments were described by only one exponential segment, with the lapilli fragments going rapidly to zero within about 50 km from the vent. The distal decay trend of coarse and that of fine ash are similar. Although this may be associated with size-selective sedimentation processes (e.g. ash aggregation, convective instabilities), it is difficult to distinguish these processes from a potential overlap of the 6th May deposit with ash from additional phases (e.g. May 2nd and May 8th) of the Chaitén eruption.

5) An accurate determination of TGSD requires a wide distribution of field observations that can describe the variation of grain size with distance from the vent across all critical shifts in fallout regimes (e.g. from lapilli to coarse ash, from coarse to fine ash). As in the case of the Chaitén eruption, when these critical parts of the deposit are not sampled (in particular when they are associated with a large mass fraction of the deposit), the addition of synthetic data located in critical areas appears to improve the TGSD estimate.

6) Our best estimate of TGSD for the climactic phase of the Chaitén 2008-20013 eruption based on the addition of critical synthetic points is uni-modal and characterized by  $Md_\phi = 2.6$  and  $\sigma_\phi = 2.5$  (dataset B). When synthetic data are not considered (dataset A), TGSD shows a pronounced bi-modality and a smaller fraction of coarse ash ( $Md_\phi = 3.6$  and  $\sigma_\phi =$

2.2). In particular, the area from 50 km to 350 km from the vent (zones Z1 and Z2) proved critical in the case of TGSD determination for the climactic phase of the Chaitén 2008-2013 eruption. Sensitivity tests also indicate that the stability of results can be reached with a small number of added synthetic data (i.e., 3-5 points per each zone, 1 every 20-45 km, for the case of the Chaitén eruption).

- 7) Due to the majority of products being sedimented in proximal area, the estimation of both erupted mass and TGSD of the climactic phase of this long-lasting eruption is not strongly affected by the possible contribution of smaller explosive events to the distal cumulative tephra deposit, which are often difficult to correlate stratigraphically. The variation of TGSD associated with a reduction of the thickness of the distal deposit (beyond 150 km from vent) to 80% and 60% of the original value result in a relatively small variation in the fraction of coarse and fine ash ( $< 5$  wt%). Alfano et al. (2011b) had already shown that a reduction of the distal thickness only resulted in the reduction of  $< 5$  wt% of erupted mass.

**Acknowledgments:** Sebastien Biass is thanked for the implementation of the Voronoi Tessellation script to describe the weight of individual polygons (<https://vhub.org/resources/329>). We thank Raffaello Cioni, Danilo M. Palladino and the Associate Editor (Jacopo Taddeucci) for their comments and suggestions that helped greatly to improve the manuscript.

## Appendix A. Determination of synthetic points and sensitivity analysis

Three large gaps in the data sampling were identified within the tephra deposit of the May 6th 2008 Chaitén eruption (Z1: 20-140 km from the vent; Z2: 260-380 km from the vent; Z3: 570-770 km from the vent; Fig. 9a of main text). Synthetic points were estimated in order to cover the lack of data in these three areas. The points were chosen along the dispersal axis and equally spaced. In order to assess the number of synthetic points required to obtain a stable TGSD, the calculation was carried out considering 3 points (Dataset B<sub>1</sub>; 1 point per zone), 9 points (Dataset B<sub>2</sub>; 3 points per zone) and 15 points (Dataset B<sub>3</sub>; 5 points per zone), respectively (Table A1). Dataset B<sub>1</sub> includes the synthetic points located in the middle of the zones (i.e, 80, 320 and 670 km from the vent for the areas Z1, Z2 and Z3, respectively). Dataset B<sub>2</sub> includes the points located at 50, 80 and 110 km from the vent for Z1; 290, 320 and 650 km from the vent for Z2; 625, 670 and 715 km from the vent for Z3. Dataset B<sub>3</sub> includes the points located at 40, 60, 80, 100 and 120 km from the vent for Z1; 280, 300, 320, 340 and 360 km from the vent for Z2; 610, 640, 670, 700 and 730 km from the vent for Z3 (Table A1).

The  $Md_{\phi}$  and the mass load of lapilli ( $X_l$ ), coarse ash ( $X_c$ ) and fine ash ( $X_f$ ) for each of these points were estimated based on the dispersal maps of Figs 6 and 7, and using the decay-trend plots of Fig. 8 of the main text. According to the observed decay trends, no lapilli particles sedimented in these areas (Fig. 8b). Based on the extrapolated grain size parameters, a synthetic GSD for each point was determined. A normal distribution was calculated based on the  $Md_{\phi}$  value for each point and using a sorting determined as the average of the values observed through the deposit (i.e. 0.4). The GSDs were then corrected for the extrapolated fraction of coarse and fine ash. The resulting GSD are shown in Fig. A1.



The GSD of the synthetic points were then used to extend the original dataset (Dataset A in Fig. 9b). Results of the TGSD associated with these 3 datasets are shown in Fig. A2. The difference of TGSD obtained using datasets  $B_2$  and  $B_3$  is small, whereas dataset  $B_1$  gives a TGSD skewed toward the coarse size fraction. We conclude that three points per zone are representative for the data gap of the climactic phase of the 2008-2013 Chaitén eruption and are sufficient to generate stable TGSD results.

## References

- Alfano F, Bonadonna C, Delmelle P, Costantini L (2011a) Insights on tephra settling velocity from morphological observations. *J Volcanol Geotherm Res* 208:86–98. doi: 10.1016/j.jvolgeores.2011.09.013.
- Alfano F, Bonadonna C, Gurioli L (2012) Insights into eruption dynamics from textural analysis: The case of the May, 2008, Chaitén eruption. *Bull Volcanol* 74:2095–2108. doi: 10.1007/s00445-012-0648-3
- Alfano F, Bonadonna C, Volentik ACM, et al (2011b) Tephra stratigraphy and eruptive volume of the May, 2008, Chaitén eruption, Chile. *Bull Volcanol* 73:613–630. doi: 10.1007/s00445-010-0428-x
- Amigo Á, Lara LE, Smith VC (2013) Holocene record of large explosive eruptions from Chaitén and Michinmahuida Volcanoes , Chile. *Andean Geol* 40:227–248. doi: 10.5027/andgeoV40n2-a
- Biass S, Bonadonna C (2014) TOTGS: Total grainsize distribution of tephra fallout. <https://vhub.org/resources/3297>.
- Bonadonna C, Cioni R, Pistolesi M, Elissondo M, Baumann V (2015) Sedimentation of long-lasting wind-affected volcanic plumes: the example of the 2011 rhyolitic Cordón Caulle eruption, Chile. *Bull Volcanol* 77:1–19. doi: 10.1007/s00445-015-0900-8
- Bonadonna C, Cioni R, Pistolesi M, Connor C, Scollo S, Pioli L, Rosi M (2013) Determination of the largest clast sizes of tephra deposits for the characterization of explosive eruptions: a study of the IAVCEI commission on tephra hazard modelling. *Bull Volcanol* 75:1–15. doi: 10.1007/s00445-012-0680-3

734 Bonadonna C, Connor CB, Houghton BF, Connor L , Byrne M, Laing A, Hincks TK (2005)  
 735 Probabilistic modeling of tephra dispersal: Hazard assessment of a multiphase rhyolitic  
 736 eruption at Tarawera, New Zealand. *J Geophys Res B Solid Earth* 110:1–21. doi:  
 737 10.1029/2003JB002896

738 Bonadonna C, Costa A (2012) Estimating the volume of tephra deposits: A new simple strategy.  
 739 *Geology* 40:415–418. doi: 10.1130/G32769.1

740 Bonadonna C, Genco R, Gouhier M, Pistolesi M, Cioni R, Alfano F, Hoskuldsson A, Ripepe M  
 741 (2011) Tephra sedimentation during the 2010 Eyjafjallajkull eruption (Iceland) from  
 742 deposit, radar, and satellite observations. *J. Geophys. Res. Solid Earth* 116: B12202,  
 743 doi:10.1029/2011JB008462.

744 Bonadonna C, Houghton BF (2005) Total grain-size distribution and volume of tephra-fall  
 745 deposits. *Bull Volcanol* 67:441–456. doi: 10.1007/s00445-004-0386-2

746 Bonadonna C, Macedonio G, Sparks RSJ (2002) Numerical modelling of tephra fallout  
 747 associated with dome collapses and Vulcanian explosions: application to hazard assessment  
 748 on Montserrat. *Geol Soc London, Mem* 21:517–537. doi:  
 749 10.1144/GSL.MEM.2002.021.01.23

750 Bonadonna C, Phillips JC (2003) Sedimentation from strong volcanic plumes. *J Geophys Res*  
 751 *Solid Earth* 108:2340. doi: 10.1029/2002JB002034

752 Brown RJ, Branney MJ, Maher C, Dávila-Harris P (2010) Origin of accretionary lapilli within  
 753 ground-hugging density currents: Evidence from pyroclastic couplets on Tenerife. *Geol Soc*  
 754 *Am Bull* 122 :305–320, doi:10.1130/B26449.1

755 Carazzo G, Jellinek AM (2013) Particle sedimentation and diffusive convection in volcanic ash-

756 clouds. *J Geophys Res Solid Earth* 118:1420–1437. doi: 10.1002/jgrb.50155

757 Carey S, Sparks RSJ (1986) Quantitative models of the fallout and dispersal of tephra from  
 758 volcanic eruption columns. *Bull Volcanol* 48:109–125. doi: 10.1007/BF01046546

759 Carey SN, Sigurdsson H (1982) Influence of particle aggregation on deposition of distal tephra  
 760 from the May 18, 1980, eruption of Mount St. Helens volcano. *J Geophys Res* 87:7061. doi:  
 761 10.1029/JB087iB08p07061

762 Carn S a., Paluster JS, Lara L, Ewert JW, Watt S, Prata AJ, Thomas RJ, Villarosa G (2009) The  
 763 Unexpected Awakening of Chaitén Volcano, Chile. *Eos (Washington DC)* 90:205–206. doi:  
 764 10.1029/2009EO240001

765 Cas RAF, Wright JV. (1988) Volcanic Successions Modern and Ancient. doi: 10.1007/978-94-  
 766 009-3167-1

767 Cashman K V, Mangan MT (1994) Physical aspects of magmatic degassing; II, Constraints on  
 768 vesiculation processes from textural studies of eruptive products. *Rev Mineral*  
 769 *Geochemistry* 30 :447–478.

770 Castro JM, Cordonnier B, Tuffen H, Mark J. Tobinf MJ, Puskarf L, Marting MC, Bechtelg HA  
 771 (2012) The role of melt-fracture degassing in defusing explosive rhyolite eruptions at  
 772 volcán Chaitén. *Earth Planet Sci Lett* 333-334:63–69. doi: 10.1016/j.epsl.2012.04.024

773 Castro JM, Dingwell DB (2009) Rapid ascent of rhyolitic magma at Chaitén volcano, Chile.  
 774 *Nature* 461:780–783. doi: 10.1038/nature08458

775 Castro JM, Schipper CI, Mueller SP, Militzer AS, Amigo A, Parejas CS, Jacob D (2013) Storage  
 776 and eruption of near-liquidus rhyolite magma at Cordón Caulle, Chile. *Bull Volcanol* 75:1–

777 17. doi: 10.1007/s00445-013-0702-9

778 Costa A, Pioli L, Bonadonna C (2016) Assessing tephra total grain-size distribution: Insights  
779 from field data analysis. *Earth Planet Sci Lett* 443:90–107. doi:  
780 <http://dx.doi.org/10.1016/j.epsl.2016.02.040>

781 Costantini L, Houghton BF, Bonadonna C (2010) Constraints on eruption dynamics of basaltic  
782 explosive activity derived from chemical and microtextural study: The example of the  
783 Fontana Lapilli Plinian eruption, Nicaragua. *J Volcanol Geotherm Res* 189:207–224. doi:  
784 10.1016/j.jvolgeores.2009.11.008

785 Dufek J, Manga M, Patel A (2012) Granular disruption during explosive volcanic eruptions. *Nat*  
786 *Geosci* 5:561–564. doi: 10.1038/ngeo1524

787 Durant AJ, Rose WI, Sarna-Wojcicki AM, Carey S, Volentik ACM (2009) Hydrometeor-  
788 enhanced tephra sedimentation: Constraints from the 18 May 1980 eruption of Mount St.  
789 Helens. *J Geophys Res* 114:1–21. doi: 10.1029/2008JB005756

790 Durant AJ (2015) Research focus: Toward a realistic formulation of fine-ash lifetime in volcanic  
791 clouds. *Geol* 43 :271–272. doi: 10.1130/focus032015.1

792 Durant AJ, Villarosa G, Rose WI, Delmelle P, Prata AJ, Viramonte JG (2012) Long-range  
793 volcanic ash transport and fallout during the 2008 eruption of Chaitén volcano, Chile. *Phys*  
794 *Chem Earth* 45-46:50–64. doi: 10.1016/j.pce.2011.09.004

795 Eychenne J, Cashman K, Rust A, Durant A (2015) Impact of the lateral blast on the spatial  
796 pattern and grain size characteristics of the 18 May 1980 Mount St. Helens fallout deposit. *J*  
797 *Geophys Res Solid Earth* 120:6018–6038. doi: 10.1002/2015JB012116

798 Eychenne J, Le Pennec JL (2012) Sigmoidal particle density distribution in a subplinian scoria  
 799 fall deposit. *Bull Volcanol* 74:2243–2249. doi: 10.1007/s00445-012-0671-4  
 800 Eychenne J, Le Pennec JL, Troncoso L, et al (2012) Causes and consequences of bimodal grain-  
 801 size distribution of tephra fall deposited during the August 2006 Tungurahua eruption  
 802 (Ecuador). *Bull Volcanol* 74:187–205. doi: 10.1007/s00445-011-0517-5  
 803 Folch A (2012) A review of tephra transport and dispersal models: Evolution, current status, and  
 804 future perspectives. *J Volcanol Geotherm Res* 235-236:96–115. doi:  
 805 10.1016/j.jvolgeores.2012.05.020  
 806 Folch A, Jorba O, Viramonte J (2008) Volcanic ash forecast – application to the May 2008  
 807 Chaitén eruption. *Nat Hazards Earth Syst Sci* 8:927–940. doi: 10.5194/nhess-8-927-2008  
 808 Genareau K, Mulukutla GK, Proussevitch A, Durant AJ, Rose WI, Sahagian DL (2013) The size  
 809 range of bubbles that produce ash during explosive volcanic eruptions. *J Appl Volcanol* 2:4.  
 810 doi: 10.1186/2191-5040-2-4  
 811 Genareau K, Proussevitch A, Durant AJ, Mulukutla GK, Sahagian DL (2012) Sizing up the  
 812 bubbles that produce very fine ash during explosive volcanic eruptions. *Geophys Res Lett*  
 813 39:1–6. doi: 10.1029/2012GL052471  
 814 Houghton BF, Wilson CJN (1989) A vesicularity index for pyroclastic deposits. *Bull Volcanol*  
 815 51:451–462. doi: 10.1007/BF01078811  
 816 Inman D (1952) Measures for describing the size distribution of sediments. *J Sediment Petrol*  
 817 125–145. doi: 10.1306/D42694DB-2B26-11D7-8648000102C1865D  
 818 Jay J, Costa F, Pritchard M, Lara L, Singer B, Herrin J (2014) Locating magma reservoirs using

819 InSAR and petrology before and during the 2011–2012 Cordón Caulle silicic eruption.  
820 Earth Planet Sci Lett 395:254–266. doi: <http://dx.doi.org/10.1016/j.epsl.2014.03.046>

821 Kaminski E, Jaupart C (1998) The size distribution of pyroclasts and the fragmentation sequence  
822 in explosive volcanic eruptions. J Geophys Res 103:29759. doi: 10.1029/98JB02795

823 Kueppers U, Perugini D, Dingwell DB (2006a) “Explosive energy” during volcanic eruptions  
824 from fractal analysis of pyroclasts. Earth Planet Sci Lett 248:800–807. doi:  
825 10.1016/j.epsl.2006.06.033

826 Kueppers U, Scheu B, Spieler O, Dingwell DB (2006b) Fragmentation efficiency of explosive  
827 volcanic eruptions: A study of experimentally generated pyroclasts. J Volcanol Geotherm  
828 Res 153:125–135. doi: 10.1016/j.jvolgeores.2005.08.006

829 Lara LE (2009) La erupcion 2008 del volcan Chaiten, Chile: informe preliminar. Andean Geol  
830 36:125–129. doi: 10.5027/556

831 Lara LE, Moreno R, Amigo Á, Hoblitt RP, Pierson TC (2013) Late Holocene history of Chaitén  
832 Volcano: New evidence for a 17th century eruption. Andean Geol 40:249–261. doi:  
833 10.5027/andgeoV40n2-a04

834 Major JJ, Pierson TC, Hoblitt RP, Moreno H (2013) Pyroclastic density currents associated with  
835 the 2008-2009 eruption of Chaitén Volcano (Chile): Forest disturbances, deposits, and  
836 dynamics. Andean Geol 40:324–358. doi: 10.5027/andgeoV40n2-a09

837 Manzella I, Bonadonna C, Phillips JC, Monnard H (2015) The role of gravitational instabilities  
838 in deposition of volcanic ash. Geol . doi: 10.1130/G36252.1

839 Martin RS, Watt SFL, Pyle DM, Mather TA, Matthews NE, Georg RB, Day JA, Fairhead T, Witt

840 MLI, Quayle BM (2009) Environmental effects of ashfall in Argentina from the 2008  
841 Chaitén volcanic eruption. *J Volcanol Geotherm Res* 184:462–472. doi:  
842 10.1016/j.jvolgeores.2009.04.010

843 Mastin LG, Guffanti M, Servranckx R, Webley P, Barsotti S, Dean K, Durant AJ, Ewert JW,  
844 Neri A, Rose WI., Schneider D, Siebert L, Stunder B, Swanson G, Tupper A , Volentik  
845 ACM, Waythomas CF (2009) A multidisciplinary effort to assign realistic source  
846 parameters to models of volcanic ash-cloud transport and dispersion during eruptions. *J*  
847 *Volcanol Geotherm Res* 186:10–21. doi: <http://dx.doi.org/10.1016/j.jvolgeores.2009.01.008>

848 Osores MS, Folch A, Collini E, Villarosa G, Durant AJ, Pujol G, Viramonte GJ (2013)  
849 Validation of the FALL3D model for the 2008 Chaitén eruption using field and satellite  
850 data. *Andean Geol* 40:262–276. doi: 10.5027/andgeoV40n2-a05

851 Perugini D, Kueppers U (2012) Fractal analysis of experimentally generated pyroclasts: A tool  
852 for volcanic hazard assessment. *Acta Geophys* 60:682–698. doi: 10.2478/s11600-012-0019-  
853 7

854 Pierson TC, Major JJ, Amigo Á, Moreno H (2013) Acute sedimentation response to rainfall  
855 following the explosive phase of the 2008-2009 eruption of Chaitén volcano, Chile. *Bull*  
856 *Volcanol* 75:1–17. doi: 10.1007/s00445-013-0723-4

857 Pyle DM (1989) The thickness, volume and grainsize of tephra fall deposits. *Bull Volcanol* 51:1–  
858 15, doi: 10.1007/BF01086757

859 Rust AC, Cashman KV. (2011) Permeability controls on expansion and size distributions of  
860 pyroclasts. *J Geophys Res Solid Earth* 116:1–17. doi: 10.1029/2011JB008494

861 Tsunematsu K, Bonadonna C (2015) Grain-size features of two large eruptions from Cotopaxi



862 volcano (Ecuador) and implications for the calculation of the total grain-size distribution.  
863 Bull Volcanol 77:1–12. doi: 10.1007/s00445-015-0949-4

864 Turcotte DL (1986) Fractals and fragmentation. J Geophys Res Solid Earth 91:1921–1926. doi:  
865 10.1029/JB091iB02p01921

866 Volentik ACM, Bonadonna C, Connor CB, Connor L, Rosi M (2010) Modeling tephra dispersal  
867 in absence of wind: Insights from the climactic phase of the 2450BP Plinian eruption of  
868 Pululagua volcano (Ecuador). J Volcanol Geotherm Res 193:117–136. doi:  
869 10.1016/j.jvolgeores.2010.03.011

870 Walker GPL (1971) Grain-Size Characteristics of Pyroclastic Deposits. J Geol 79:696–714. doi:  
871 10.2307/30065501

872 Watt SFL, Gilbert JS, Folch A, Phillips JC, Cai XM (2015) An example of enhanced tephra  
873 deposition driven by topographically induced atmospheric turbulence. Bull Volcanol 77:1–  
874 14. doi: 10.1007/s00445-015-0927-x

875 Watt SFL, Pyle DM, Mather T, Martin RS, Matthews NE (2009) Fallout and distribution of  
876 volcanic ash over Argentina following the May 2008 explosive eruption of Chaitén, Chile. J  
877 Geophys Res Solid Earth 114:1–11. doi: 10.1029/2008JB006219

878 Watt SFL, Pyle DM, Naranjo J, Rosqvist G, Mella M, Mather TA, Moreno H (2011) Holocene  
879 tephrochronology of the Hualaihue region (Andean southern volcanic zone, ~42° S),  
880 southern Chile. Quat Int 246:324–343. doi: 10.1016/j.quaint.2011.05.029

881 Wicks C, de la Llera JC, Lara LE, Lowenstern J (2011) The role of dyking and fault control in  
882 the rapid onset of eruption at Chaitén volcano, Chile. Nature 478:374–377. doi:  
883 10.1038/nature10541

884 Wilson TM, Stewart C, Sword-Daniels V, Leonard GS, Johnston DM, Cole JW, Wardman J,  
885 Wilson G, Barnard ST (2012) Volcanic ash impacts on critical infrastructure. *Phys Chem*  
886 *Earth, Parts A/B/C* 45–46:5–23. doi: <http://dx.doi.org/10.1016/j.pce.2011.06.006>  
887 Wohletz K, Sheridan M, Brown W (1989) Particle size distribution and the sequential  
888 fragmentation/transport theory applied to volcanic ash. *J Geophys Res* 94:15–703, doi:  
889 10.1029/JB094iB11p15703  
890  
891

## Figure captions

**Figure 1.** a) Location of Chaitén volcano. b) isopach maps (in cm) of the May 6th 2008 deposit ( $\beta$  layer) in the proximal area (modified after Alfano et al 2011b), indicating the location of the samples analysed in this work (red points indicate samples that were also processed for componentry analysis. c) Isopach map (in cm) of the May 6th 2008 deposit ( $\beta$  layer) in the distal area (modified after Alfano et al (2011b)) and indicating the location of the sample points (black diamonds; Watt et al (2009)); isopach contours are obtained extrapolating the thickness values from the total deposit map of Alfano et al (2011b) and accounting for possible overlap of multiple depositional phases; black dashed line encloses the depositional area of the explosive activity of May 3rd-5th.

**Figure 2.** Density distribution plot showing the values obtained through high precision water pycnometer analysis. Black diamonds indicate the average value of the measurements, error bars indicate the standard deviation; the grey line indicate the bulk density of the lithic samples; the reddish area indicate the values of density measured for the pumice clasts (Alfano et al 2011b); the black dashed line indicate a hypothetical sigmoidal distribution (Eycheenne and Le Pennec 2012) that would be expected for a sample composed of juvenile vesicular clasts that would show a trend with density increasing as the grain size decreases.

**Figure 3.** a) Map showing selected distal sites of the Chaitén 2008-2013 deposit, and their relationship with the major explosive phases and plume transport directions (gray arrows) during the eruption. The May 6th phase is affected by overlap with deposit from May 2nd and May 8th. b) Grain-size distributions of selected sites ~150 km from source, showing the notably coarser population attributed to the May 6th plume. c) Down-wind patterns in grain-size distributions in the May 6th deposit. The coarse population (shaded areas) is attributed to May 6th, while the

finer mode potentially includes some component of additional eruption phases (May 2nd, 8th). d) SEM images of ash samples from the distal Chaitén deposit.

**Figure 4.** Grain-size distribution and componentry histograms.  $Md_\phi$  and  $\sigma_\phi$  of bulk samples are indicated; the red curves, where present, indicate the subpopulation identified through SFT analysis; plots not showing red curves refer to samples whose SFT deconvolution resulted in a single population.

**Figure 5.** a) Plot of  $Md_\phi$  versus distance from the vent for bulk samples of the proximal and distal sites referred to the May 6th deposit. b) Plot of  $Md_\phi$  versus  $\sigma_\phi$  where the dashed line indicates the fallout field (modified after Walker (1971)); the plot includes values for the bulk samples of proximal and distal sites, and the mode and dispersion values of coarse and fine subpopulations identified in the proximal samples from deconvolution analysis.

**Figure 6.** Isoline maps of  $Md_\phi$  (a), and mass load ( $\text{kg/m}^2$ ) of lapilli (b), coarse ash (c) and fine ash (d) in the proximal area.

**Figure 7.** Isoline maps of  $Md_\phi$  (a), and mass load ( $\text{kg/m}^2$ ) of coarse ash (b), and fine ash (c) in the distal area.

**Figure 8.** Decay trend vs. the distance from the vent along the dispersal axis of  $Md_\phi$  of bulk samples (a), and mass load of lapilli (b), coarse ash (c) and fine ash (d) fractions. Shaded areas indicate the sampling gap zones Z1, Z2 and Z3 (cf. Fig. 9). The plot for Lapilli clasts (b) includes a zoomed plot to better show the trend in the proximal area.

**Figure 9.** Total grain size distribution. a) Voronoi tessellation associated with the combination of the original dataset and the additional 9 synthetic points (i.e. polygons with red outline) (dataset B). Colours show the absolute mass associated with individual polygons (i.e. mass/area of samples multiplied by polygon area); c) TGSD results associated with the individual datasets.

**Figure 10.** Comparison of the TGSD associated with the dataset B with TGSD associated with the original dataset A, datasets C, D, E and F (obtained selectively removing the synthetic points of Z1, Z2, Z3, Z1+Z2, respectively), and datasets G and H (obtained reducing the mass load values of the distal points, beyond 150 km from the vent, to 80 % and 60 %, respectively).

**Figure 11.** a) Variation of the GSD-PND power-law exponents with distance from the vent; b) Cumulative Log-Log plots of TGSD-PND, obtained from the Voronoi tessellation using datasets A (regression line:  $y = 2.7 \cdot 10^5 x^{-3.1}$ ,  $R^2 = 0.98$ ) and B (regression line:  $y = 3 \cdot 10^5 x^{-3.0}$ ,  $R^2 = 0.98$ ) (Fig. 8c), and Conv-PND (regression line:  $y = 4.5 \cdot 10^5 x^{-2.9}$ ,  $R^2 = 0.99$ ), obtained by convoluting the GSD-PND trends; c) Cumulative Log-Log plot comparing TGSD-PND associated with dataset B together with the VSD (regression line:  $y = 6.0 \cdot 10^5 x^{-3.1}$ ,  $R^2 = 0.98$ ) estimated for the pumice samples (Alfano et al 2012). The vertical axis indicates the number of particles, referred to TGSD-PND, and the number of vesicles, referred to the VSD.

**Figure A1.** Plots showing the GSD derived for each synthetic point selected the areas Z1, Z2 and Z3 (Table A1).

**Figure A2.** Plot showing the TGSD derived for datasets B<sub>1</sub>, B<sub>2</sub> and B<sub>3</sub> containing 3, 9 and 15 points, respectively

Figure 1

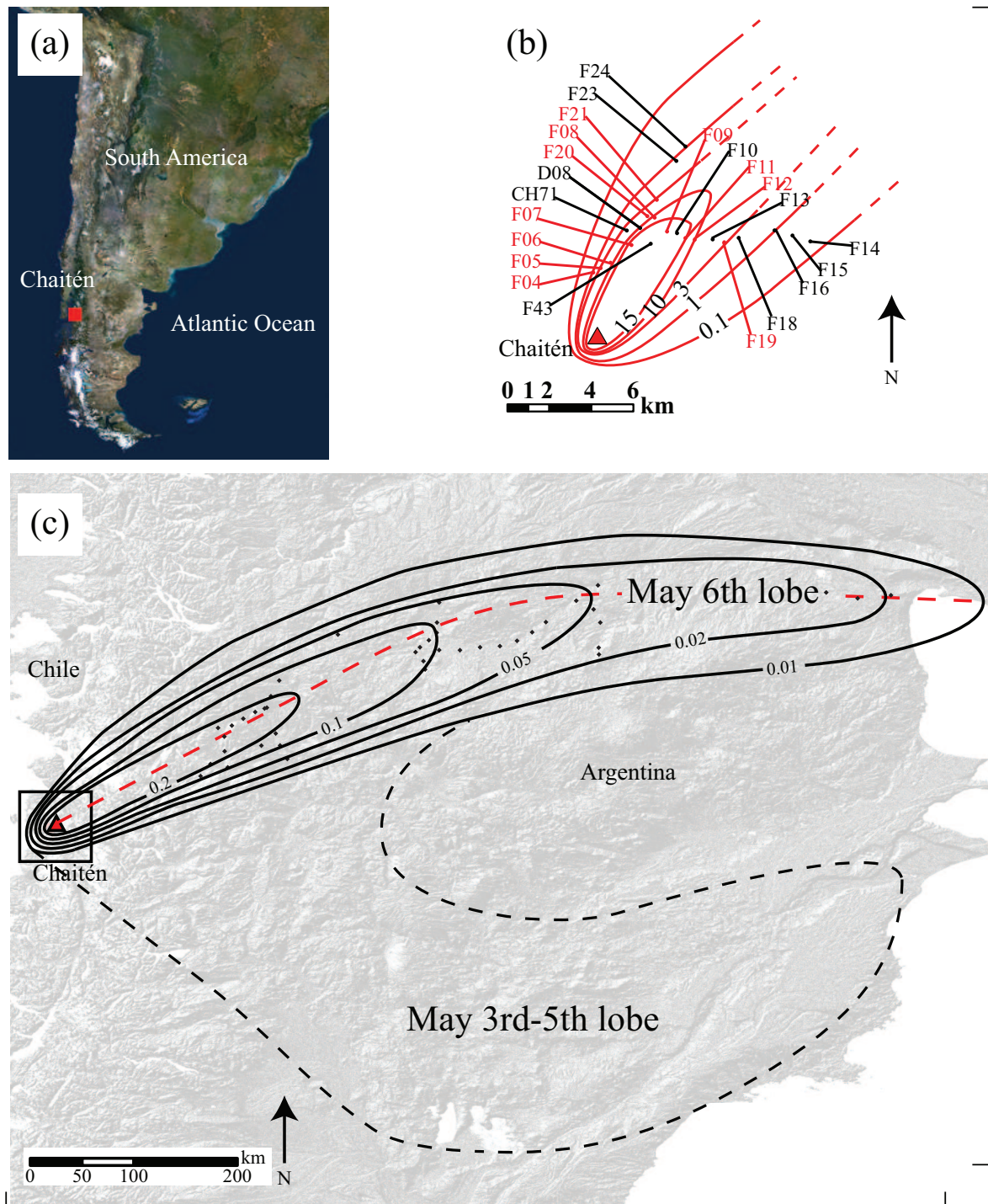


Figure 2

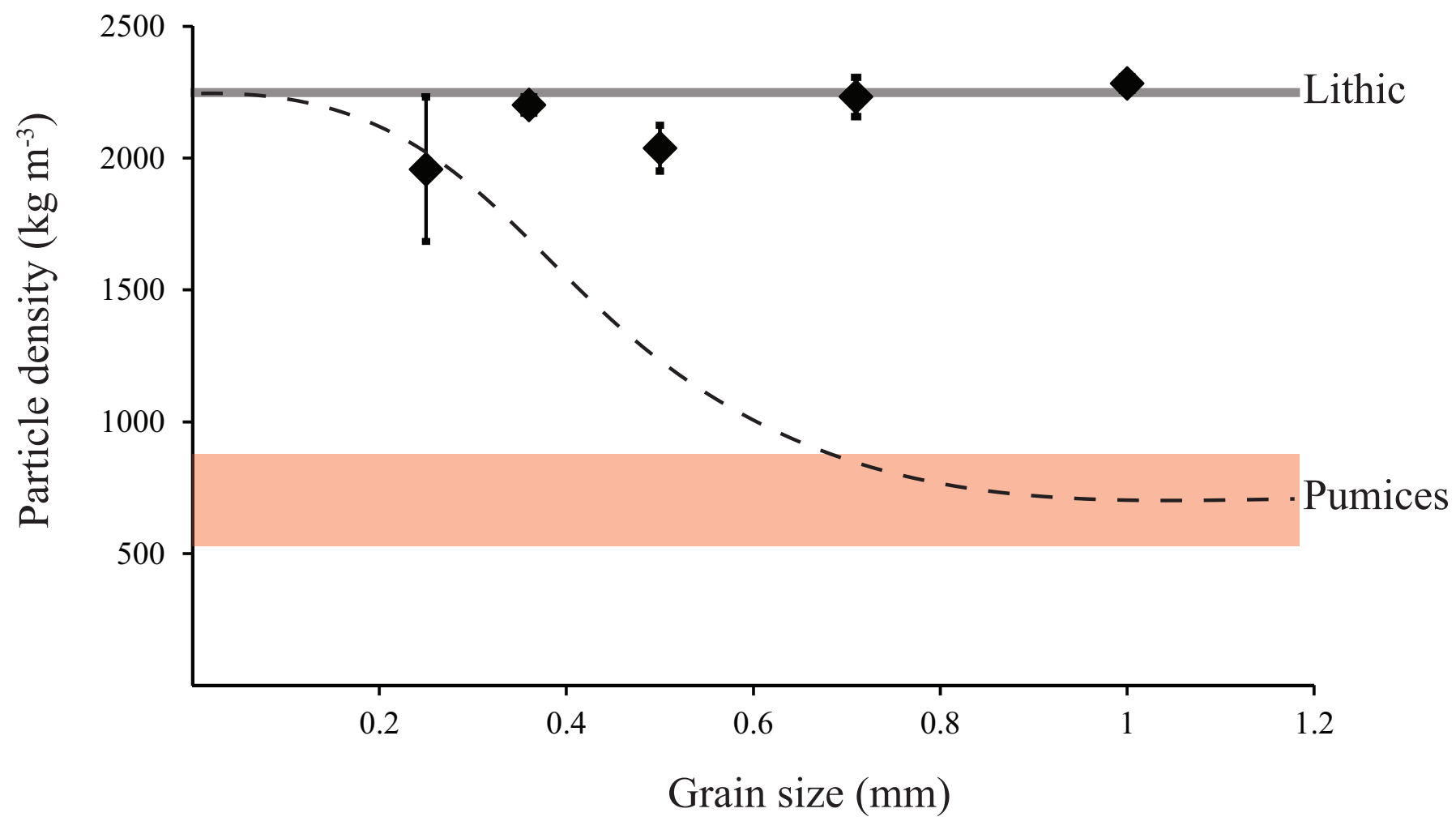




Figure 3

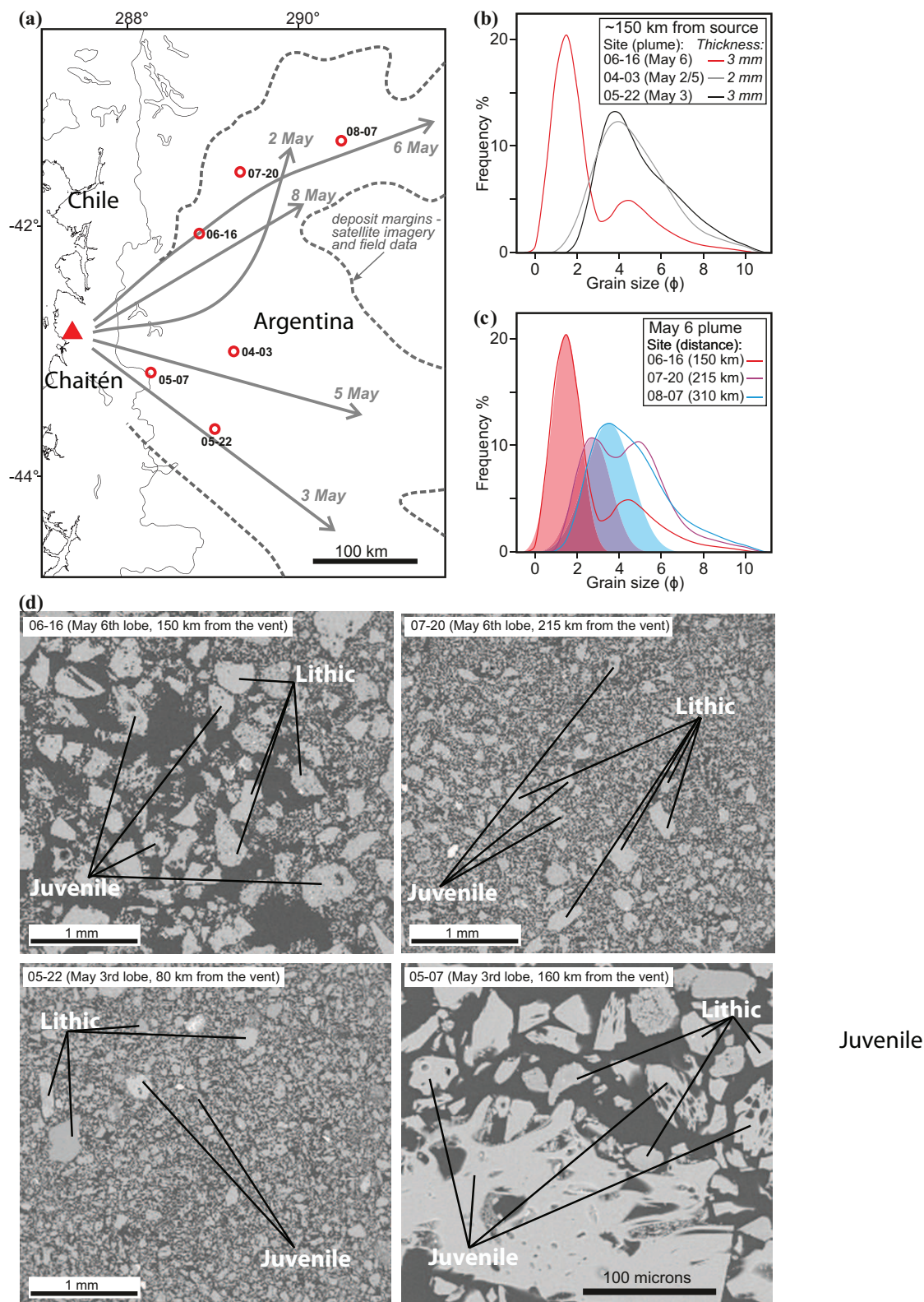
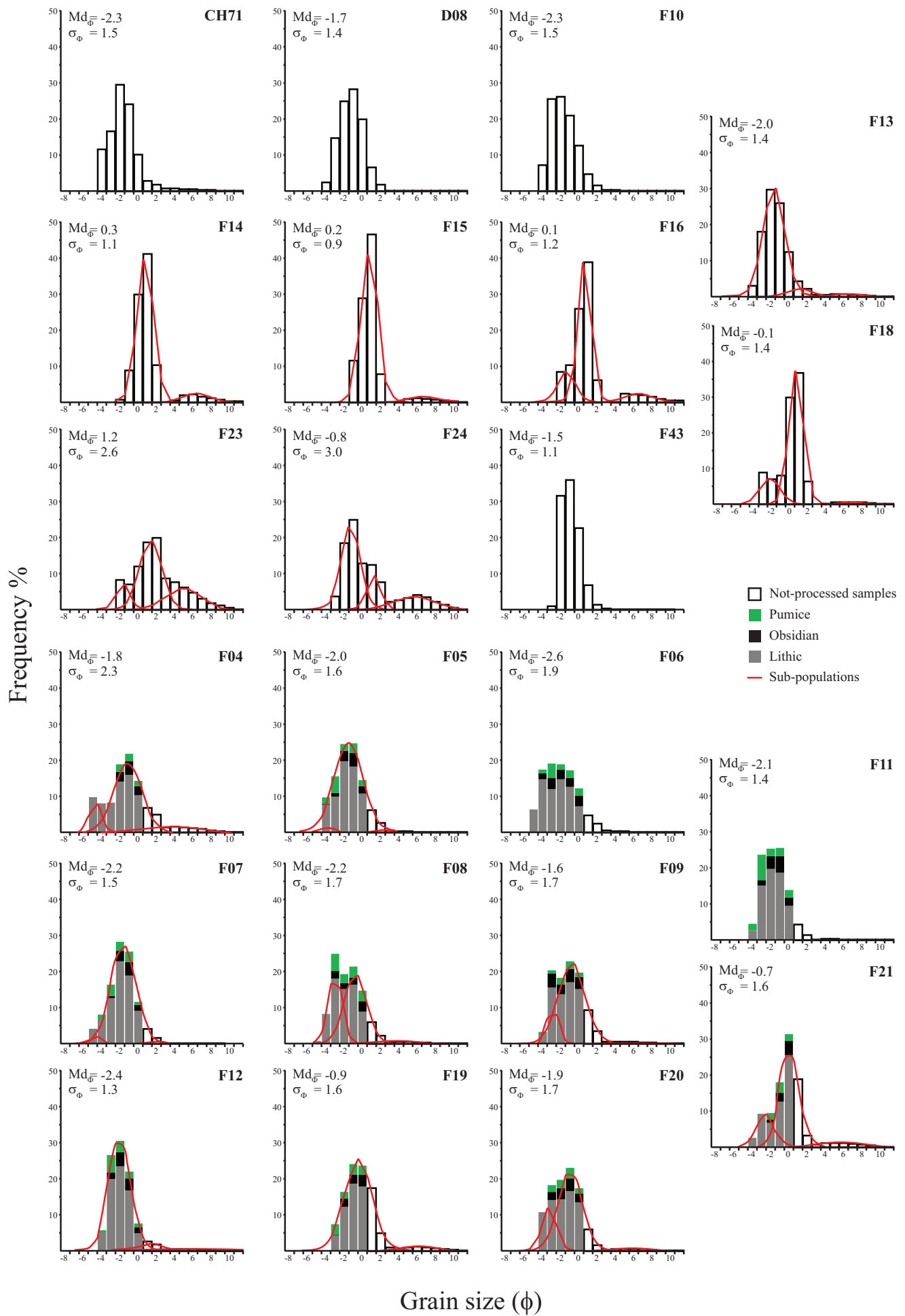
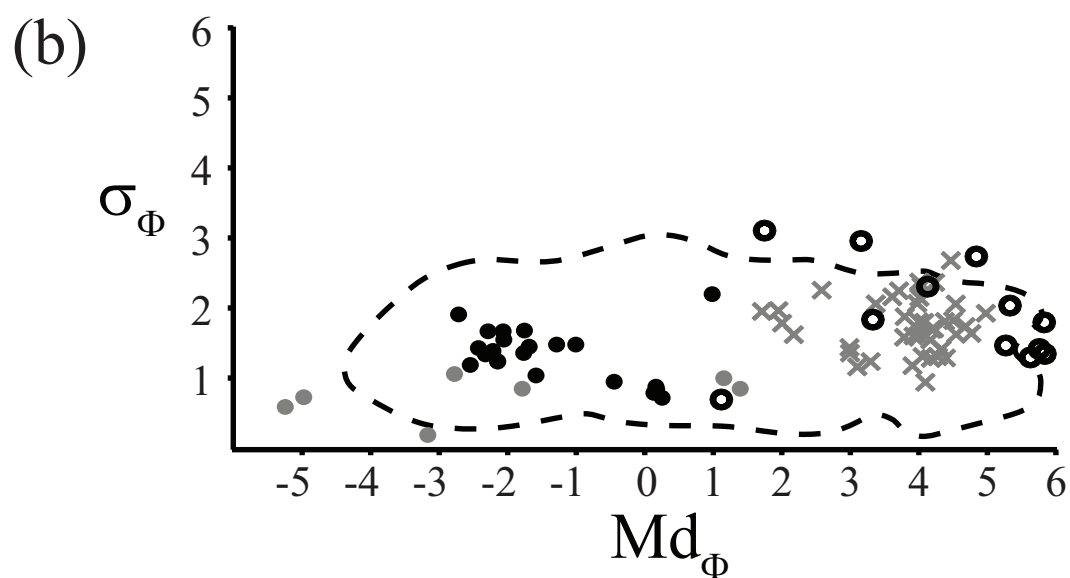
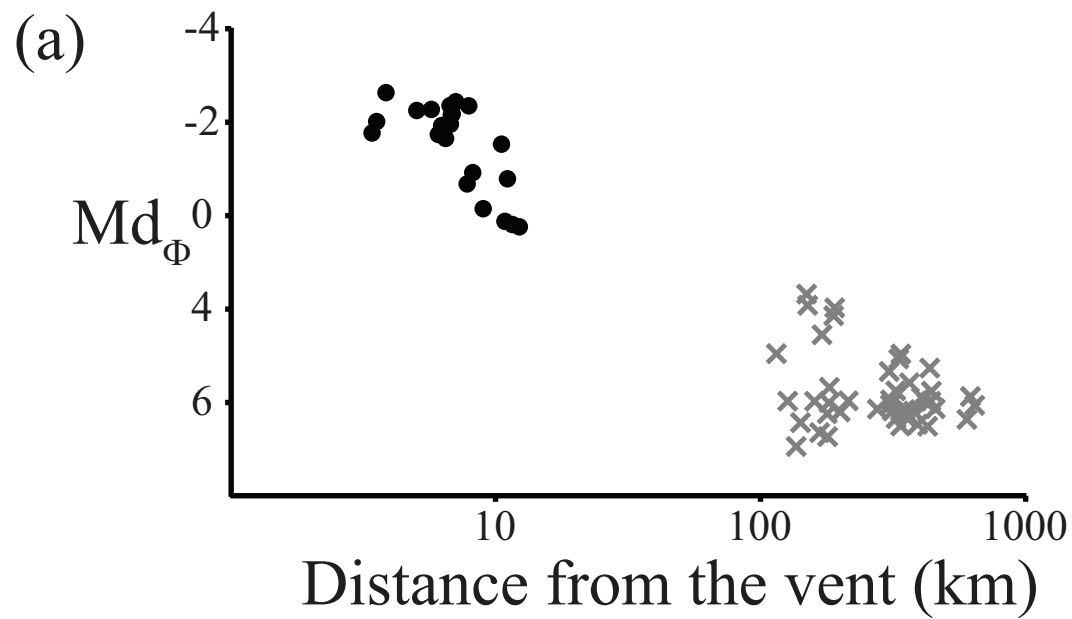




Figure 4





Bulk sample values

- Proximal sites
- × Distal sites [*Watt et al.*, 2009]

Secondary sub-populations identified  
in the proximal samples

- Coarse sub-population
- Fine sub-population

Figure 6

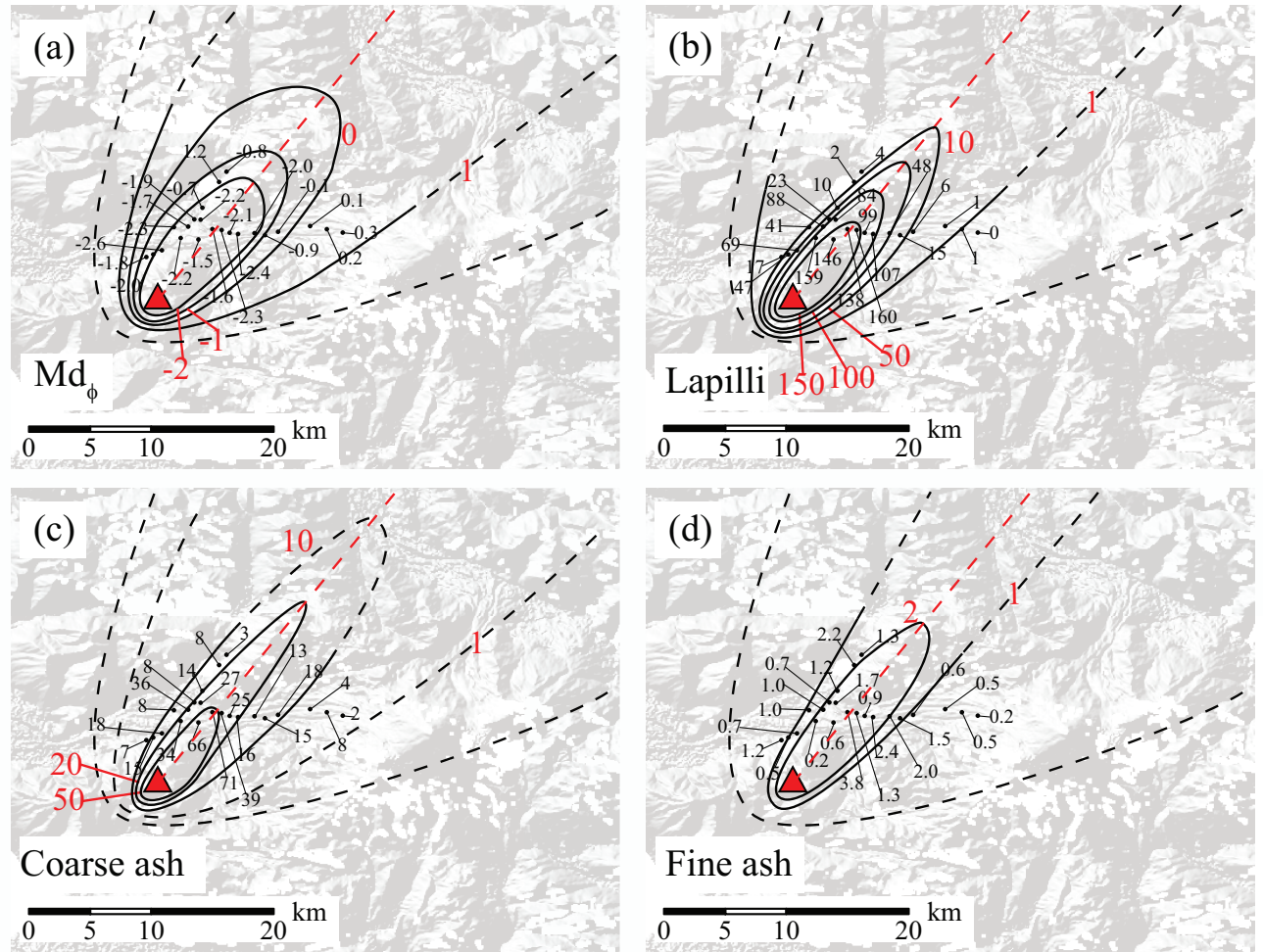


Figure 7

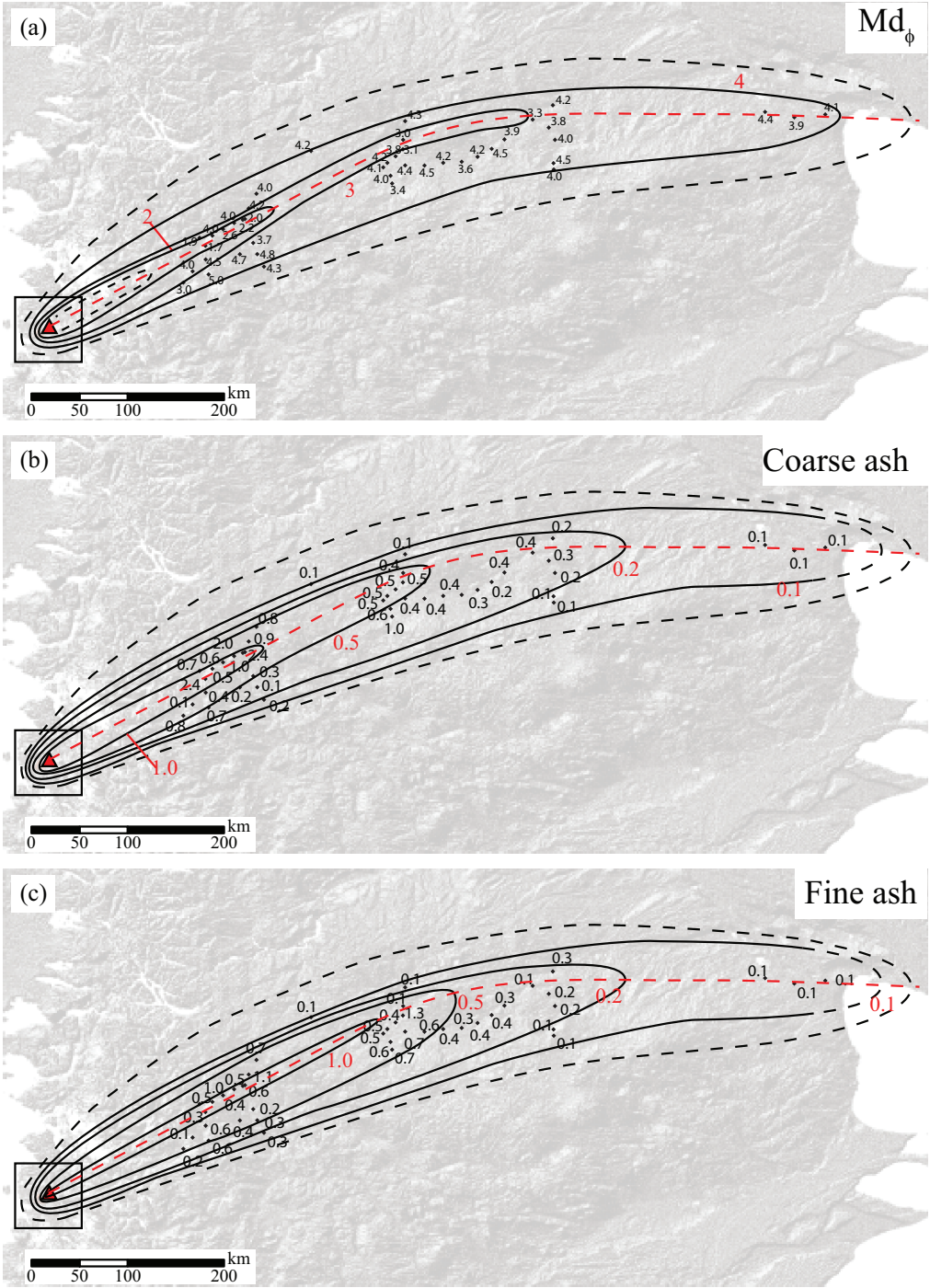


Figure 8

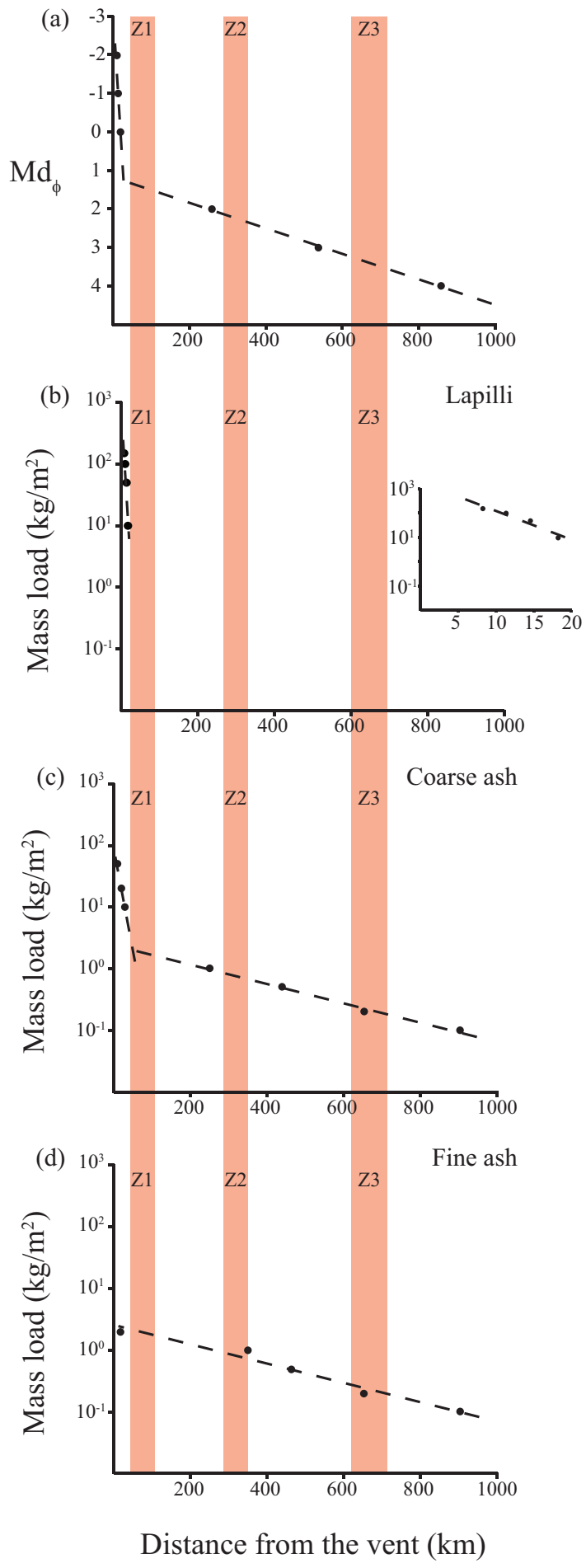




Figure 9

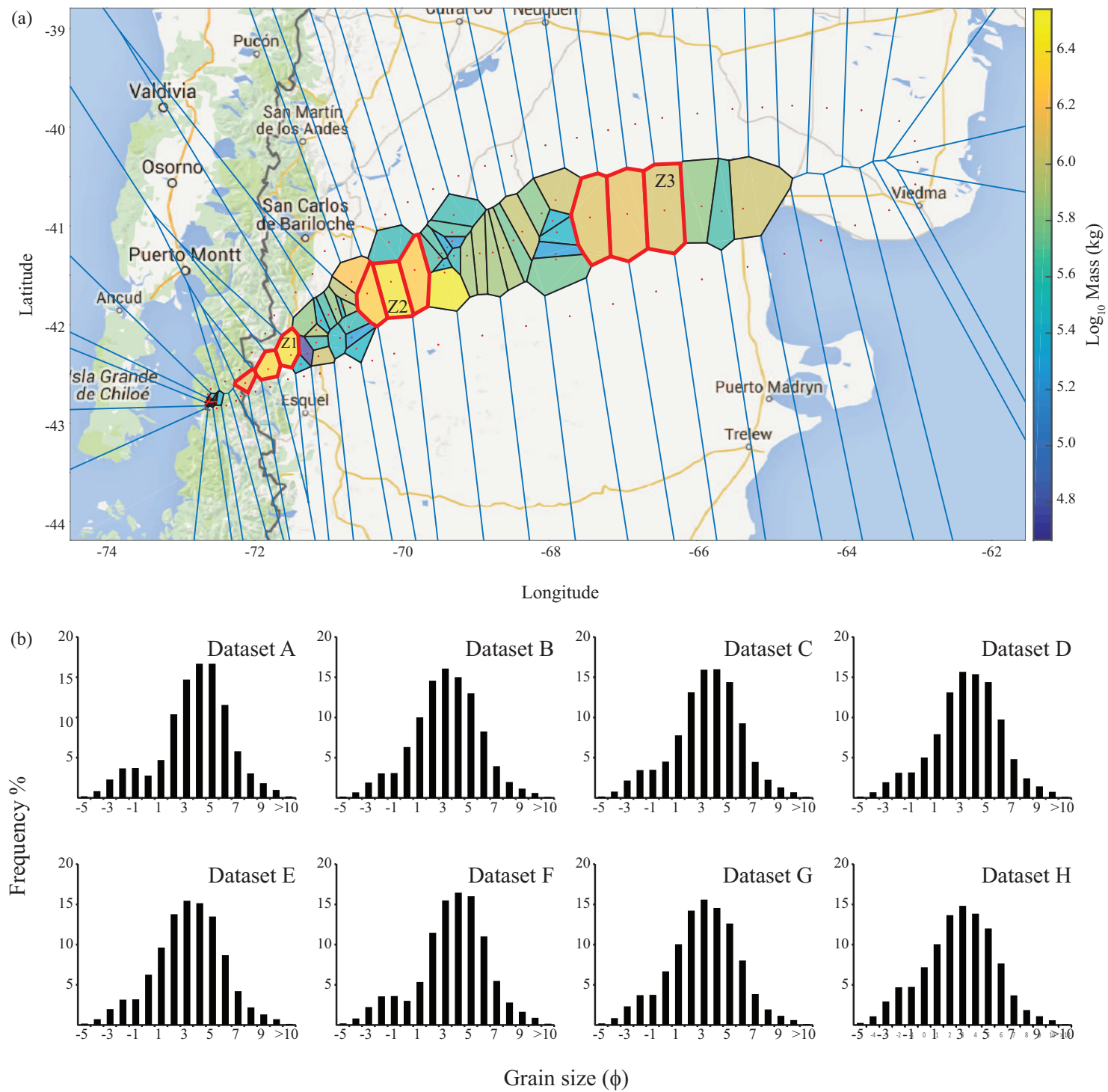


Figure 10

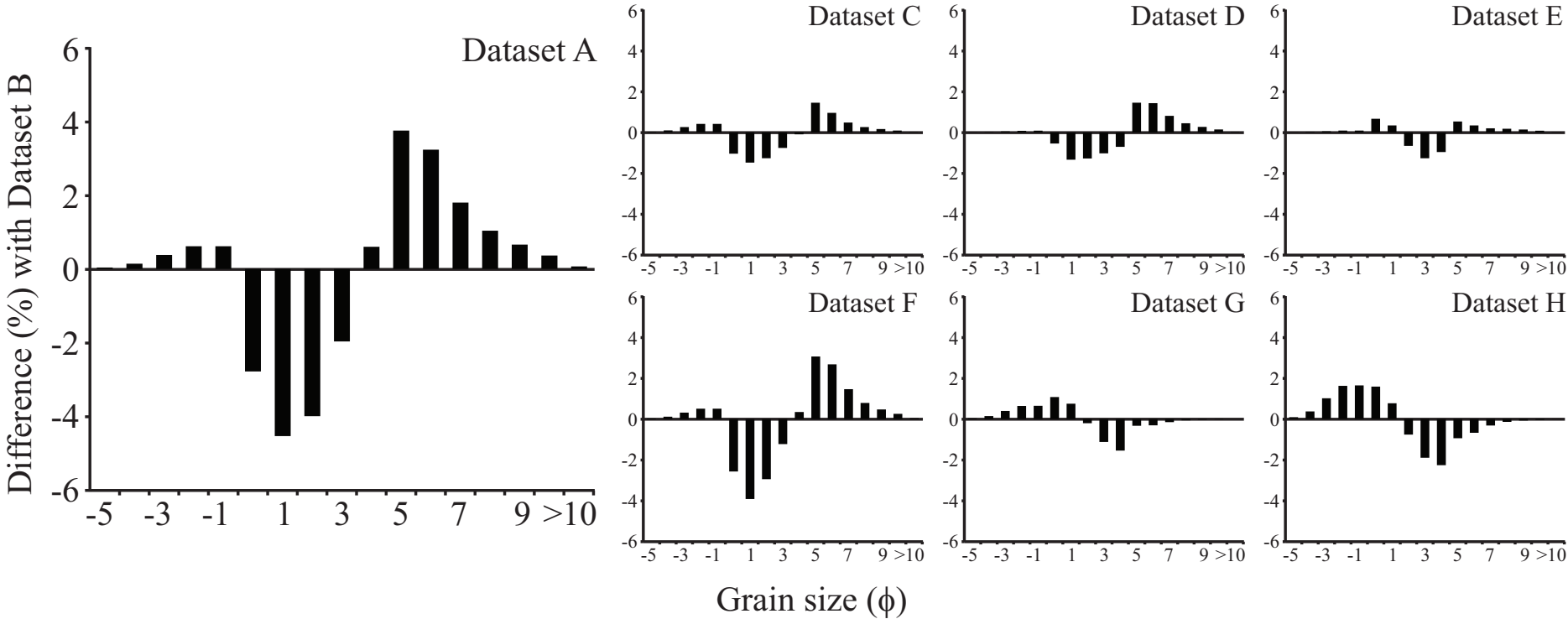
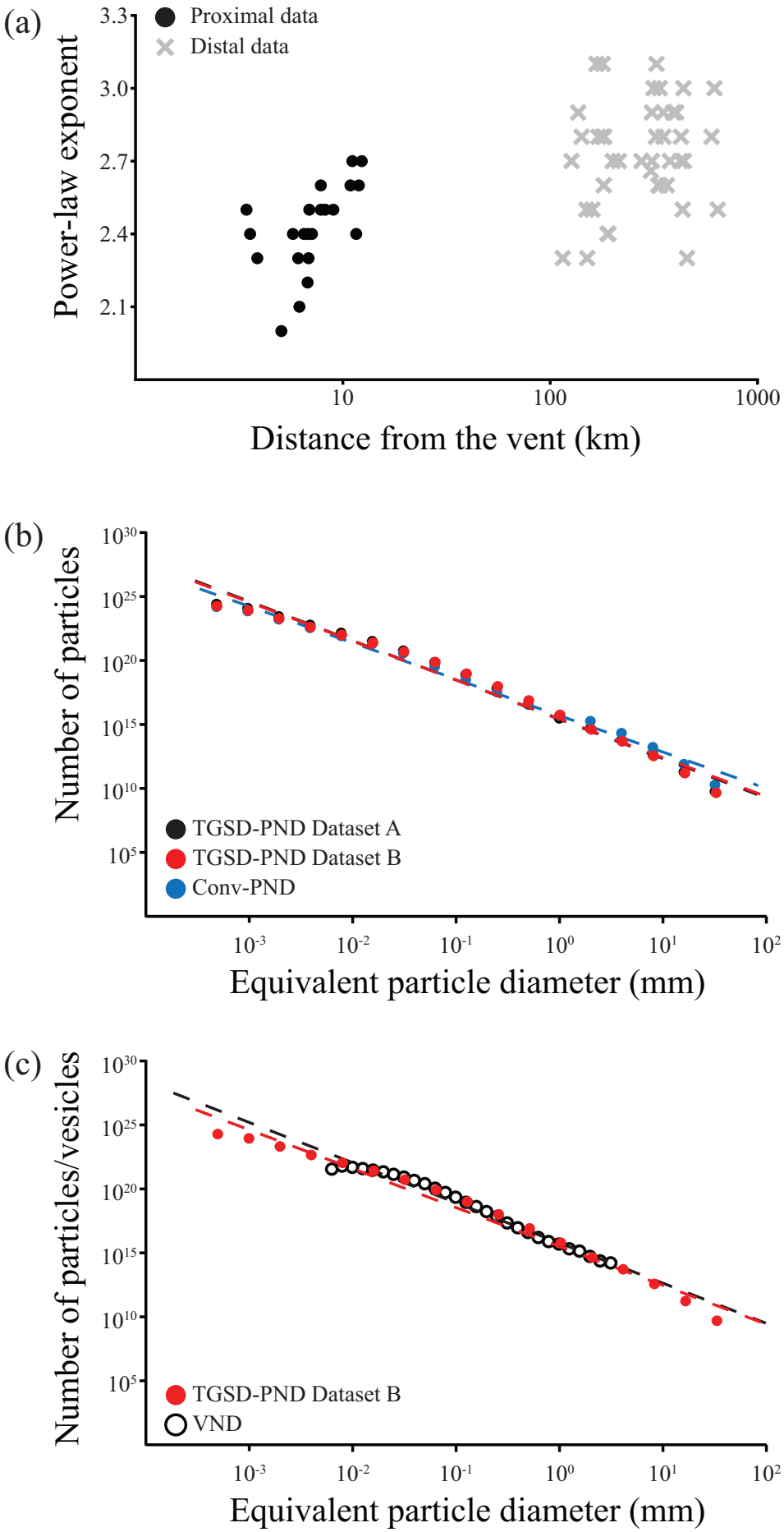


Figure 11





**Table 1.** List and composition of the datasets used to compute the TGSD.

| Dataset | Composition   |
|---------|---|
| A       | Includes sample data of the proximal and distal deposit and no synthetic points |
| B       | Dataset A integrated with 9 synthetic points (3 for each gap zone)              |
| C       | Dataset A integrated with 6 synthetic points (3 for Z2 and 3 for Z3)            |
| D       | Dataset A integrated with 6 synthetic points (3 for Z1 and 3 for Z3)            |
| E       | Dataset A integrated with 6 synthetic points (3 for Z1 and 3 for Z2)            |
| F       | Dataset A integrated with 3 synthetic points for Z3                             |
| G       | Dataset B with mass load of the distal points reduced to 80%                    |
| H       | Dataset B with mass load of the distal points reduced to 60%                    |

Figure A1

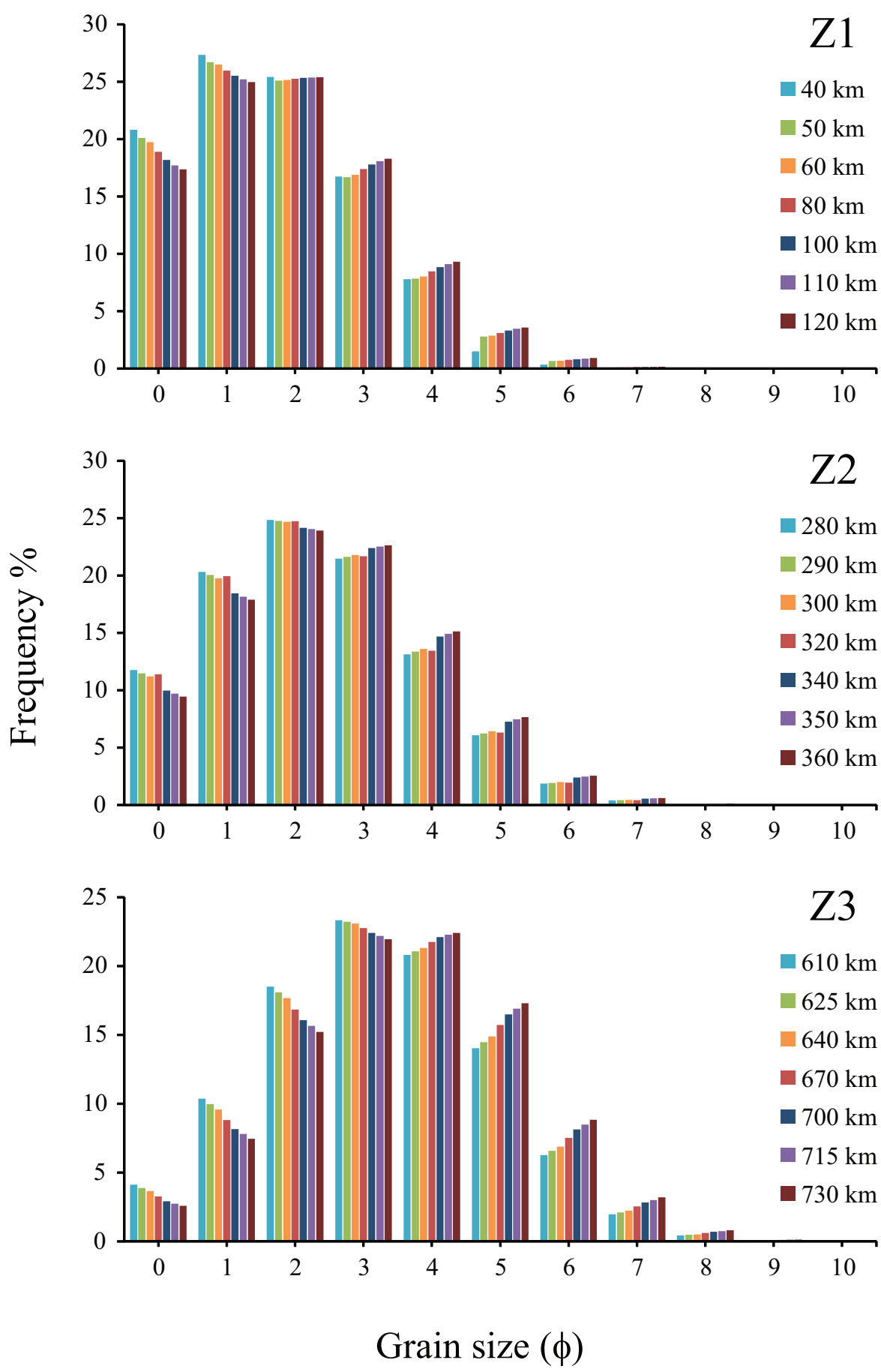
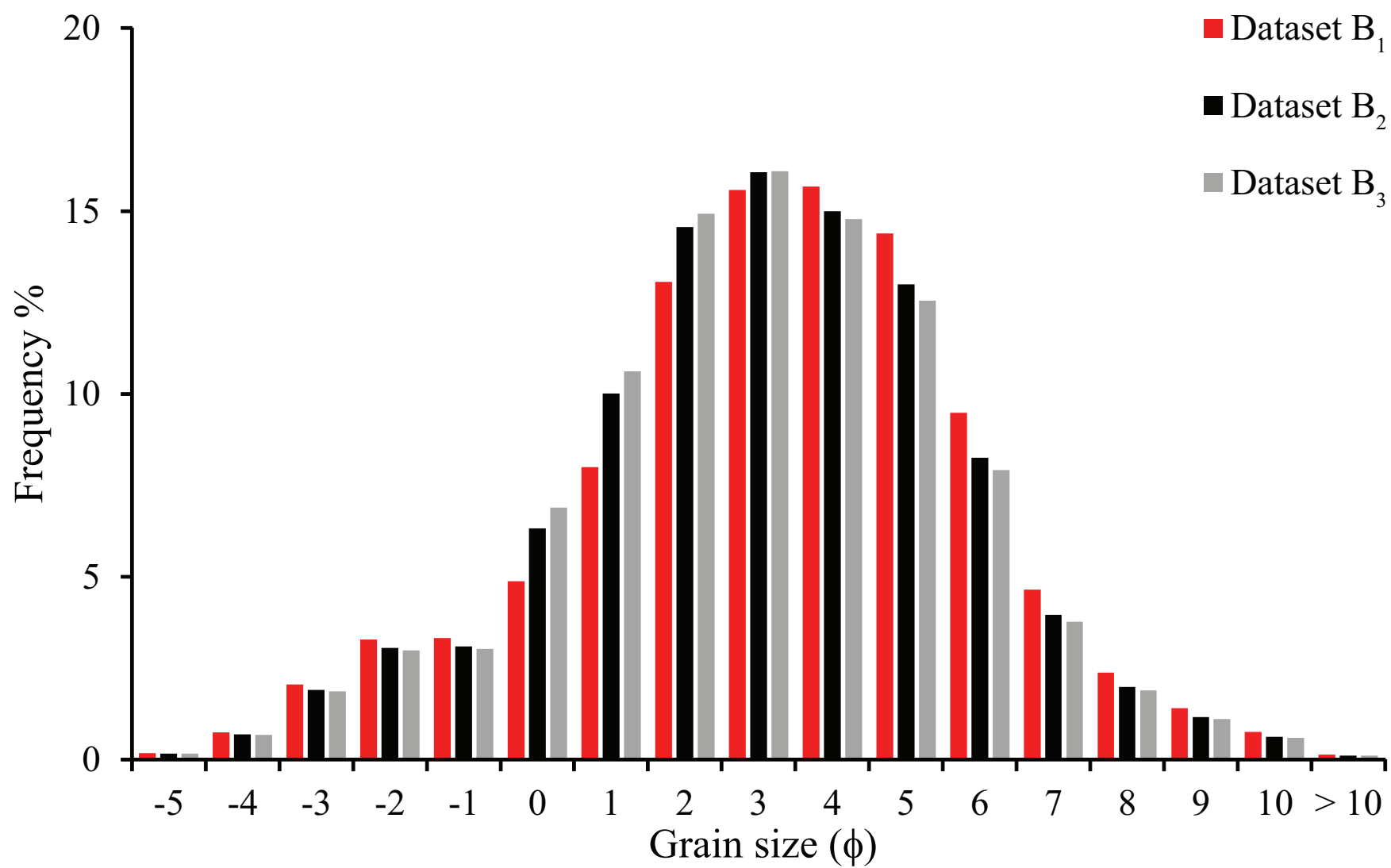
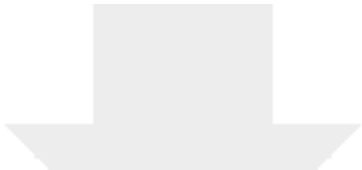


Figure A2

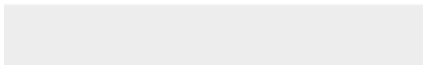
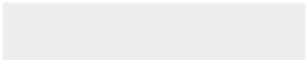


**Table A1.** Description of synthetic points where the distance from the vent (D, km) and values of  $Md_\phi$ ,  $X_c$  and  $X_f$  fraction, and mass load (M; kg/m<sup>2</sup>) are reported. Z1, Z2 and Z3 indicate the 3 critical areas of Fig. 9a.

|           | Z1  |     |     |     |     |     |     | Z2  |     |     |     |     |     |     | Z3  |     |     |     |     |     |     |
|-----------|-----|-----|-----|-----|-----|-----|-----|-----|-----|-----|-----|-----|-----|-----|-----|-----|-----|-----|-----|-----|-----|
| D         | 40  | 50  | 60  | 80  | 100 | 110 | 120 | 280 | 290 | 300 | 320 | 340 | 350 | 360 | 610 | 625 | 640 | 670 | 700 | 715 | 730 |
| $Md_\phi$ | 1.3 | 1.3 | 1.4 | 1.4 | 1.5 | 1.5 | 1.6 | 2.1 | 2.1 | 2.1 | 2.2 | 2.3 | 2.3 | 2.3 | 3.2 | 3.2 | 3.3 | 3.4 | 3.5 | 3.5 | 3.6 |
| $X_c$     | 3.7 | 1.9 | 1.9 | 1.7 | 1.6 | 1.5 | 1.5 | 0.8 | 0.7 | 0.7 | 0.7 | 0.6 | 0.6 | 0.5 | 0.2 | 0.2 | 0.2 | 0.2 | 0.1 | 0.1 | 0.1 |
| $X_f$     | 2.1 | 2.1 | 2.0 | 1.8 | 1.7 | 1.6 | 1.6 | 0.8 | 0.8 | 0.8 | 0.7 | 0.6 | 0.6 | 0.6 | 0.2 | 0.2 | 0.2 | 0.2 | 0.2 | 0.1 | 0.1 |
| M         | 5.9 | 4.0 | 3.8 | 3.5 | 3.3 | 3.1 | 3.0 | 1.6 | 1.5 | 1.5 | 1.4 | 1.3 | 1.2 | 1.2 | 0.4 | 0.4 | 0.4 | 0.3 | 0.3 | 0.3 | 0.3 |



[Click here to access/download](#)  
**Supplementary Material**  
SM1.pdf





Click here to access/download  
**Supplementary Material**  
SM2.xlsx

